Full Waveform Analysis of Ground Penetrating Radar Measurements

A DISSERTATION

SUBMITTED TO THE FACULTY OF THE GRADUATE SCHOOL

OF THE UNIVERSITY OF MINNESOTA

BY

Yuejian Cao

IN PARTIAL FULFILLMENT OF THE REQUIREMENTS

FOR THE DEGREE OF

Doctor of Philosophy

Joseph Labuz, Bojan Guzina

August, 2011

Acknowledgements

I wish to express my sincerely gratitude to my advisors for their patience and guidance in helping me to obtain this degree.

I am also grateful to Seechew Soon, Qing Lin and other graduate students for their contribution during my time in graduate school.

I also would like to thank my parents and family for their endless support during the study.

Dedication

To my love, Feili Hong.

Abstract

The purpose of this study is to extend the use of ground penetrating radar methodology towards a more reliable and accurate interpretation of pavement conditions. First, a complete set of 3D layered electromagnetic Green's functions is derived by way of transverse electric and transverse magnetic scalar potentials, featuring a new "direct" formulation for the field forms of the spectral Green's functions. The improper integrals underpinning the computation of the corresponding point-load solutions in the spatial domain are evaluated via the method of asymptotic decomposition, wherein the singular behaviors are entirely extracted and integrated analytically – so that the remaining residual components can be computed effectively and accurately via adaptive numerical quadrature. It is also found that, in the spectral domain, the decay of the (numerically-integrated) residual field forms is commensurate to that of their potential-form counterparts, which eliminates the perceived gap between the computation of the field forms and respective potential forms of the Green's functions in the spatial domain. The effectiveness and accuracy of the proposed methodology is evaluated via comparison with relevant examples in the literature. Second, utilizing the derived electromagnetic Green's function for a layered system due to a horizontal electric dipole, the GPR scan

can be simulated over a wide range of pavement profiles. Examples are provided for GPR simulation on a three-layer pavement system. By virtue of this forward model, the best match of the GPR scan in terms of the full waveform can be recovered within thousands of simulations via a optimization routine, where the *in-situ* layer parameters associated with the measurement are found to be equal to the simulation inputs. The accuracy of the interpreted layer thickness from the proposed scheme is verified by ground truth, with average error around 2.3% compared to 7.5% average error for the traditional method. In addition, the proposed scheme allows an evaluation of the relevant pavement properties with no prior assumptions or subjective image adjustments, unlike the traditional method.

Contents

List of Tables

List of Figures

Chapter 1

Introduction

Among the rapidly growing number of field techniques and devices used to evaluate near- and sub-surface conditions of transportation facilities, ground penetrating radar (GPR) is a technique of mounting popularity owing to its superior rate (*i.e.* speed) of field coverage. Most GPR applications revolve around the estimation of layer thickness using the travel-time technique, where the layer thickness is delineated by the time marker in the received signal, as shown in Fig. 1.1.

Owing to the inherent benefits such as fast, near-continuous field coverage and low implementation cost, GPR surveys have been gaining popularity among transportation agencies. The travel-time technique has been successfully applied to pavement analysis for the evaluation of a road profile. In a typical GPR image, as shown in Fig. 1.2, all the scans (in vertical direction) are stacked together

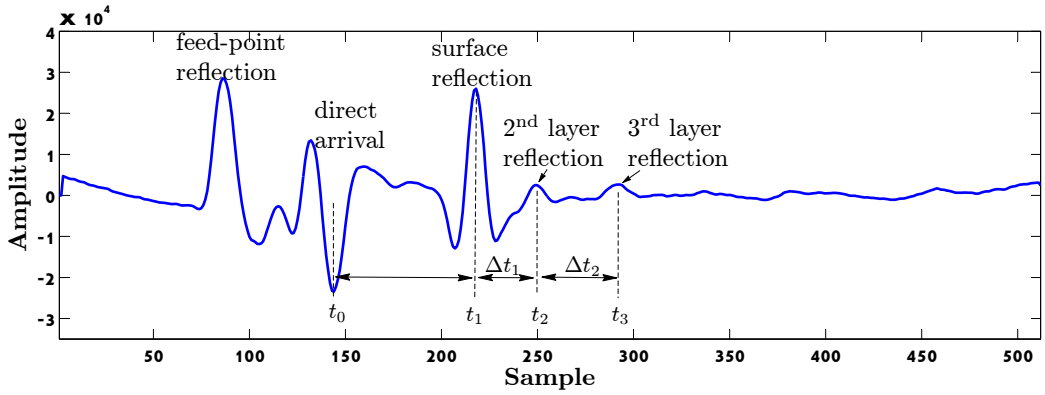

Figure 1.1: Single scan from a GPR survey.

to display the pavement profile along the road. The apparent layer profile is clearly displayed, with the top dotted line indicating the surface, the second and third dotted lines denoting the bottoms of the top two layers, and the incomplete dotted line representing possible deterioration of the deeper layer. With user-specified gain adjustment of time histories (vertical lines in Fig. 1.2) via the post-processing software, GPR is capable of picking up the variation of both top and deeper layers. Thus, the continuous coverage and fast data collection make GPR technique an effective technique for pavement applications provided that images are suitably manipulated through gain adjustments. In this setting, however, it must be recognized that the vertical axis in Fig. 1.2 is actually travel time, which is converted to depth assuming the wave speed (*i.e.* the dielectric constant) in each layer.

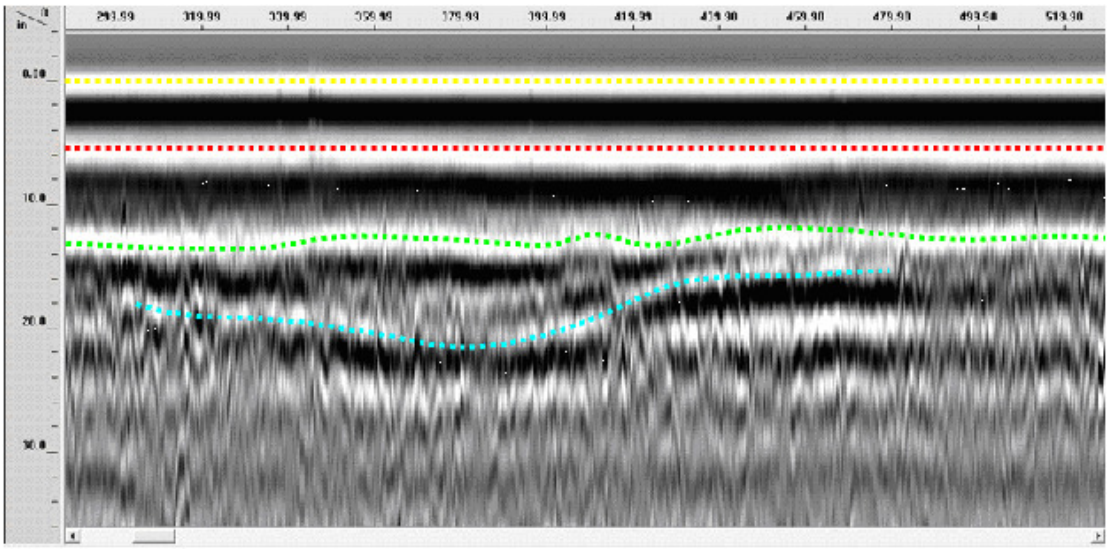

Figure 1.2: GPR image from a road survey.

The-state-of-practice GPR applications revolve around the estimate of layer thickness using the travel time technique, where the layer is delineated by the time marker in the received signal. Because the pulse travels back and forth within the pavement structure, the layer thickness h is computed as the product of the travel time Δt and the pulse velocity v inside the layer:

$$h = v\frac{\Delta t}{2}, \tag{1.1}$$

where v is related to the speed of light in vacuum c via the dielectric constant ε of the layer:

$$v = \frac{c}{\sqrt{\epsilon}}. \tag{1.2}$$

In this setting (the traditional travel-time technique), the dielectric constants

(ϵ) and travel time (Δt) are the information needed to find the layer thickness, as shown in (1.1) and (1.2). The travel time technique has been successfully applied to evaluate the pavement profile [4, 5, 6, 7]. However, the value of ϵ is usually assumed in practice, which has been shown to be inconsistent with the *in-situ* values from case to case. In fact, the assumed dielectric is often taken from empirical knowledge, which degrades the accuracy of the layer thickness estimation. In addition, since each peak in the temporal GPR record represents a pulse reflected back from a layer interface, during the field survey, the peak may be overwhelmed by the ambient noise, thus multiplying the difficulty of identifying the travel time between interfaces. This latter problem is often dealt with by user-specified gain adjustment applied to selected portions of the time histories. Although improvements can be made by implementing additional surveys to determine the *in-situ* dielectric constant [8] or calibrating through field cores, it is merely a trade-off that reduces the benefits of the GPR technique.

Furthermore, it is known that layer properties are governed not only by dielectric constants, but also the magnetic permeability and electrical conductivity. Although in the scope of pavement engineering, materials generally belong to the non-magnetic kind with the magnetic permeability identical to that in air, the electrical conductivity can vary for the different materials [5]. It is important to note the dissipation of electromagnetic wave energy during propagation occurs

because of conductivity, meaning that the GPR signal attenuates more in a higher conductive material. Unfortunately, attenuation is generally not considered in a standard interpretation.

As a consequence of these sources of error, layer thickness determined by traditional travel-time technique is to a large extent an approximation. The state-of-practice in estimating the layer thickness has an error around without calibration to cores [9]. The error may be reduced by acquiring additional information to estimate the *in-situ* conditions [8]. Nevertheless, no attenuation factor is considered in such estimation for dielectric constant, which still hampers the accuracy to interpret the GPR survey.

Delamination between hot-mix asphalt (HMA) layers is a critical degradation mechanism in HMA pavements. A number of cases have been studied that show a pavement with delamination experiences premature damage [2]. Furthermore, theoretical studies have shown the effect of poor bonding on asphalt pavement performance [3]. A delamination is essentially a separation or discontinuity in the pavement, where fracture mechanics provides the necessary criteria to predict initiation and propagation of the delamination, which can lead to other forms of distress such as stripping and pavement deformation. An accurate nondestructive testing technique to determine the presence and size of the delamination would be beneficial in developing an economical rehabilitation strategy.

To provide a rational basis for the economic management of pavements, development of a high-resolution diagnostic tool capable of detecting and quantifying the gradual degradation of HMA would be beneficial. To this end, the focus of this study is to develop an accurate, nondestructive technique for the near-surface characterization of HMA pavements based on a full waveform analysis that would simultaneously interpret the wave velocity and attenuation measurements within the framework of a multi-layered (pavement) system.

To improve the-state-of-practice GPR technique, notice that the information about the preassigned layer condition, *i.e.* the dielectric constant and conductivity, is actually contained in the amplitude information. The key point is how to incorporate the amplitude analysis of the full waveform (*i.e.* the electromagnetic measurement) into the back-analysis. As a matter of fact, a rigorous model about the electromagnetic wave propagation in the layered system is neccessary as the first step to tackle the back-analysis problem, as will be illustrated in Chapter 3. After that, in Chapter 4, the back-analysis based on the full waveform including both the amplitude and travel time information will be discussed. The interpreted layer properties from the field GPR measurements are also presented and examined in Chapter 4.

Chapter 2

Traditional GPR Analysis

In this chapter, the capabilities and limitations of ground penetrating radar (GPR) for use in local roadway applications will be demonstrated through the analysis of the regular implementation. The effectiveness of a GPR survey is a function of site conditions, the equipment used, and experience of personnel interpreting the results. This chapter will give a brief overview of GPR equipment and its usage. It will helpful to understand the potential GPR applications for use on local roads, and assist in determining what site conditions are appropriate for using GPR. In addition, not all site conditions are appropriate for GPR applications, as will be listed later.

The GPR technique has an advantage over other non-destructive techniques in that the source and receiver do not need to be attached to the pavement; this

arrangement is referred to as an air-coupled antenna and allows surveys to be performed near highway speed. The Minnesota Department of Transportation (MnDOT) has two such antennas that operate at 1.0 or 2.0 GHz and these penetrate 0.6-1 m into the ground. To improve resolution, a ground-coupled antenna can be used at walking speed and MnDOT has such three antennas: 100, 400, and 1,500 MHz, with the 100 MHz antenna penetrating 3-6 m into the ground. A GPR image shown in Fig. 2.1 is developed by combining a number of time histories obtained during the survey. The GPR image reflects certain features due to either the road surface or underground objects. In order to better understand and interpret GPR images, several ideal GPR images associated with certain features are reviewed. It is important to note that the image is different from the road profile.

GPR has been used successfully in a variety of roadway applications, including: (1) measuring layer thickness of asphalt pavements and granular base layers; (2) estimating asphalt densities; (3) determining moisture content of base materials; (4) identifying stripping zones in asphalt layers; (5) detecting buried objects such as metal pipes and near-surface bedrock. These applications are discussed in a detailed reports which contains 22 projects completed throughout the State of Minnesota [10]. The surveys included pavement thickness and profile evaluation (12 projects), void detection (7 projects), and utility location (3 projects).

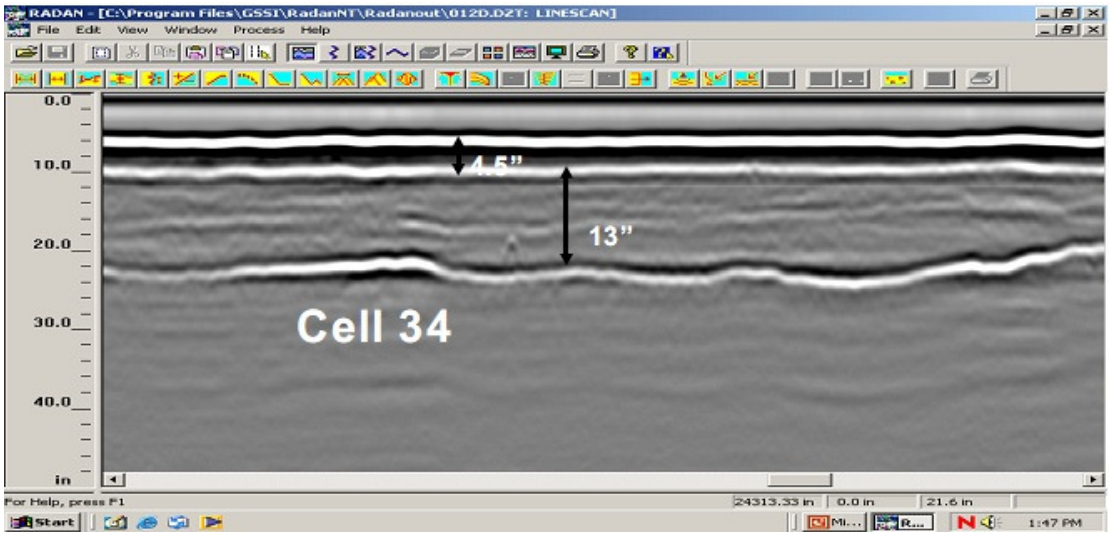

Figure 2.1: GPR image obtained from Cell 34 at MnROAD. The asphalt layer was estimated to be 0.11 m. and the base thickness was 0.33 m.

In general, the GPR technique was successful in pavement thickness and profile evaluation. However, it has some problems with void detection. Special existing conditions that should be avoided because they may interfere with the GPR signal include

- standing water or snow on the highway,
- high-ground water conditions,
- use of cellular phones,
- nearby transmission towers (noisy signals),
- metal reinforcement near-surface, or materials containing high contents of

iron ore bearing rock (e.g., taconite).

2.1 Pavement Thickness

The GPR technique is an effective tool to evaluate asphalt pavement thickness and the near surface profile. In particular, GPR is usually successful in estimating depths (less than a few feet) of the pavement structure over long distances (several miles). Figure 2.2 illustrates a depression on the surface of the road that may be caused by rutting or other form of pavement distress. Figures 2.3(a) and 2.3(b) are the resulting GPR images for a ground- and air-coupled antenna.

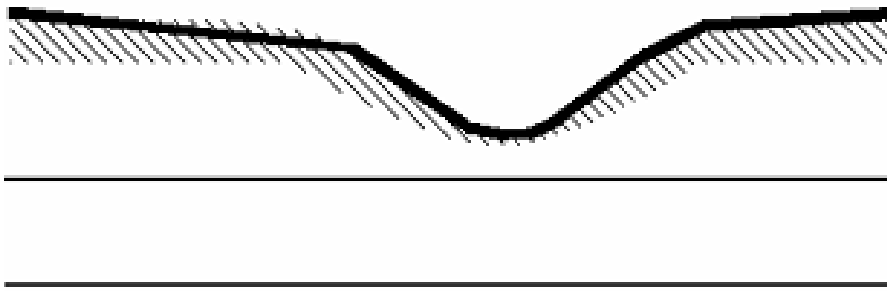

Figure 2.2: Sketch of a pavement profile.

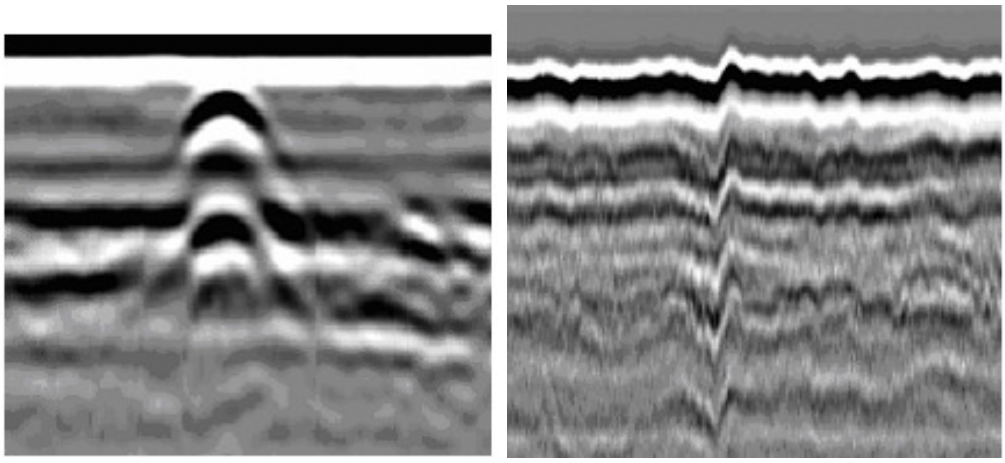

(a) (b)

Figure 2.3: GPR image from (a) ground-coupled and (b) air-coupled antenna surveying a road with a depression.

Pavement thickness evaluation is based on the measurement of the time difference between layer reflections and knowing the propagation velocity (or equivalently, the dielectric constant) within each layer. The reflections from the interfaces must be strong enough to be interpreted and tracked for reasonably consistent results. The American Society for Testing and Materials (ASTM) Standard D 4748-87 presents detailed procedures for determining the thickness of pavements using GPR. For data collection at normal highway speeds, an air coupled antenna (1.0 or 2.0 GHz) is attached to a vehicle and a collection density of 9.8 scans/m is used, with a penetration depth of approximately 0.76 m. Experience has shown that GPR works well on flexible pavements (asphalt) where there is a strong dielectric contrast between layers, but may be less effective on rigid pavements

(concrete) where the presence of moisture tends to attenuate the radar signal, or where the contrast between layers is minimal such as between concrete and granular base materials. Despite limitations associated with weak signals and material dielectric uncertainties, the advantages of determining thickness with GPR are considerable, since it is a nondestructive, continuous, and high-speed field test. Thus, using GPR technology to determine pavement layer thickness is appropriate for asphalt pavements and dry concrete roadways. It is not appropriate for evaluating wet, high-clay content subgrade layers. Figure 2.1 is an example of the high-quality data that can be obtained.

Another example to estimate the thickness is the GPR survey performed on CSAH 37 south of Erskine in Polk County. The objective of the survey was to identify the variation of an overlay and pavement thickness. The survey length was 9.8 km using a 2.0 GHz air-coupled antenna. A GPR image is shown in Figure 8; the horizontal dimension is feet and the vertical dimension is depth below the road surface. The white horizontal line at a vertical depth of 0 m. is the road surface (indicated by yellow dashed line). The red and green dashed lines indicate the bottom of the overlay and bottom of the surface layer, respectively as shown in Fig. 2.4. For this project, the overlay depth varied from $3.8 \sim 7.6$ cm, with an average of 4.3 cm and a standard deviation of 0.25 cm. The surface layer depth varied from $6.3 \sim 12.7$ cm, with an average of 8.9 cm and a standard deviation of

1.3 cm. The pavement profile is shown in Fig. 2.5.

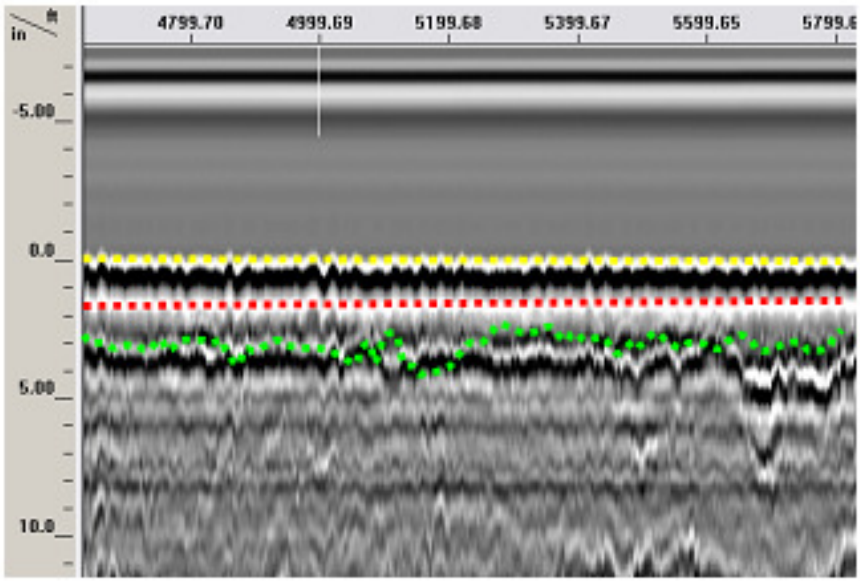

Figure 2.4: GPR image from CASH37.

2.2 Profile Evaluation

Subsurface anomalies such as a void (cavity) or an obstacle (metal pipe), as shown in Fig. 2.6, may be detected using GPR. For example, a void can develop because of consolidation, subsidence, or erosion of the base material. Generally, voids occur beneath joints where water enters the layer and carries out fines. In theory, voids filled with air or water are both detectable using GPR because the dielectric constants of air (1.0) and water (81) are substantially different than most pavement materials (3-10). If the void is air-filled, a large negative peak will appear

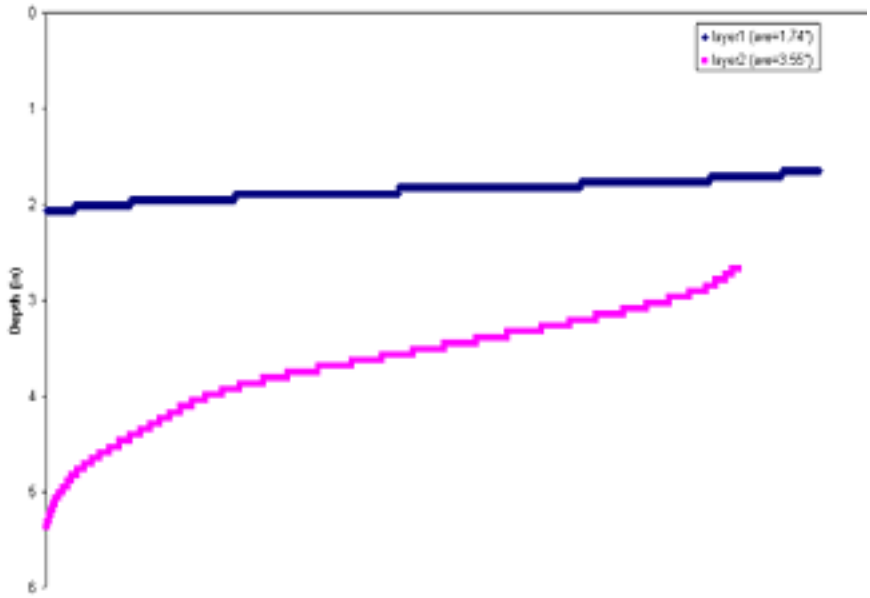

Figure 2.5: CASH37 pavement thickness.

in the waveform, and the resulting GPR image appears as multiple hyperbole as illustrated in Fig. 2.7(a), wherein a metal object is a perfect reflector and one hyperbole appears in the image as shown in Fig. 2.7(b).

Both the void and utilities detection are succefully illustrated in the 22 projects. The void detection is nicely illustrated by a GPR image of buried culverts as shown in Fig. 2.8, where multiple hyperbole identify the buried pipe. Utilities such as water pipe or other metal object can be located if sufficient penetration is achieved. MnROAD provided an opportunity to probe a pavement where metal plates were placed 0.27 and 0.43 m. below the surface. As shown in Fig. 2.9, a single hyperbole is associated with each metal plate.

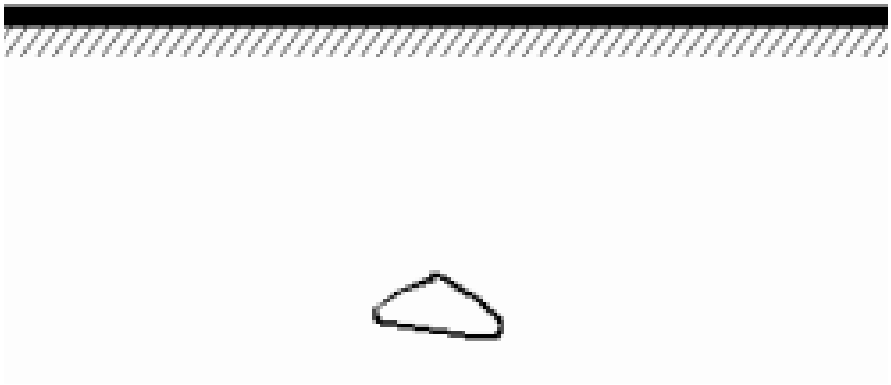

Figure 2.6: Sketch of object that represents (a) void (Fig. 2.7(a)) or (b) obstacle (Fig. 2.7(b)).

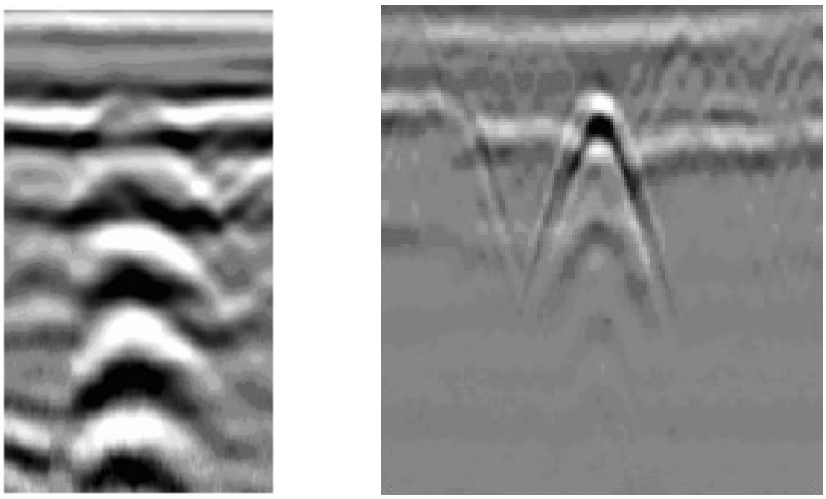

(a) (b)

Figure 2.7: GPR image (a) void; (b) obstacle.

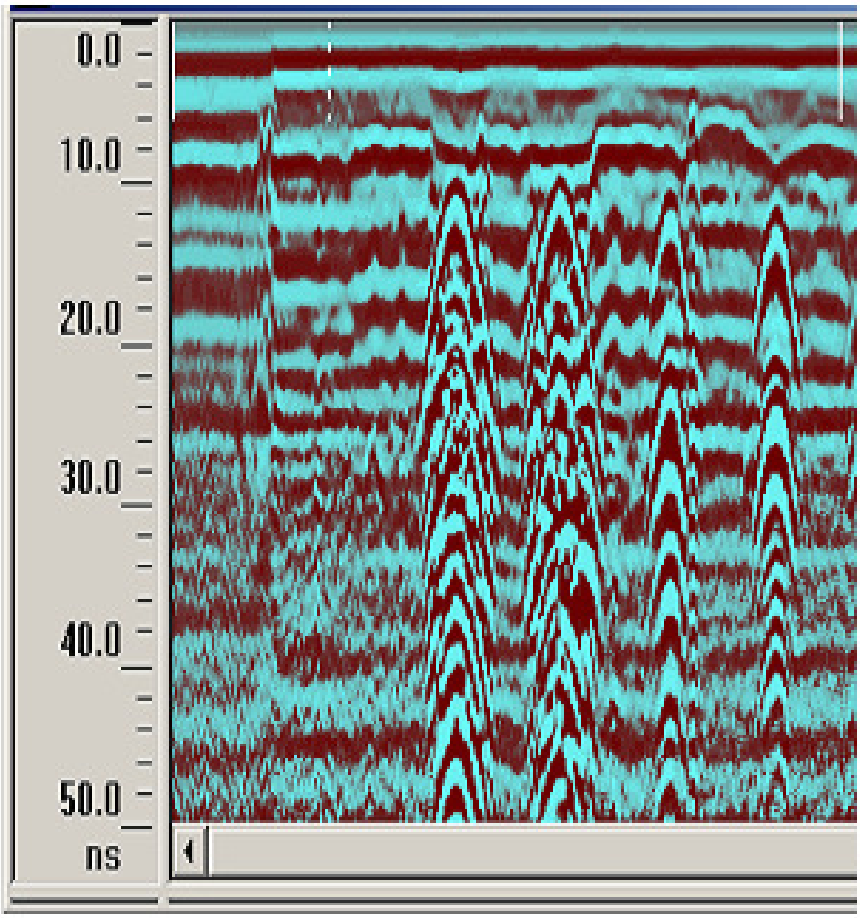

Figure 2.8: GPR image from buried culverts.

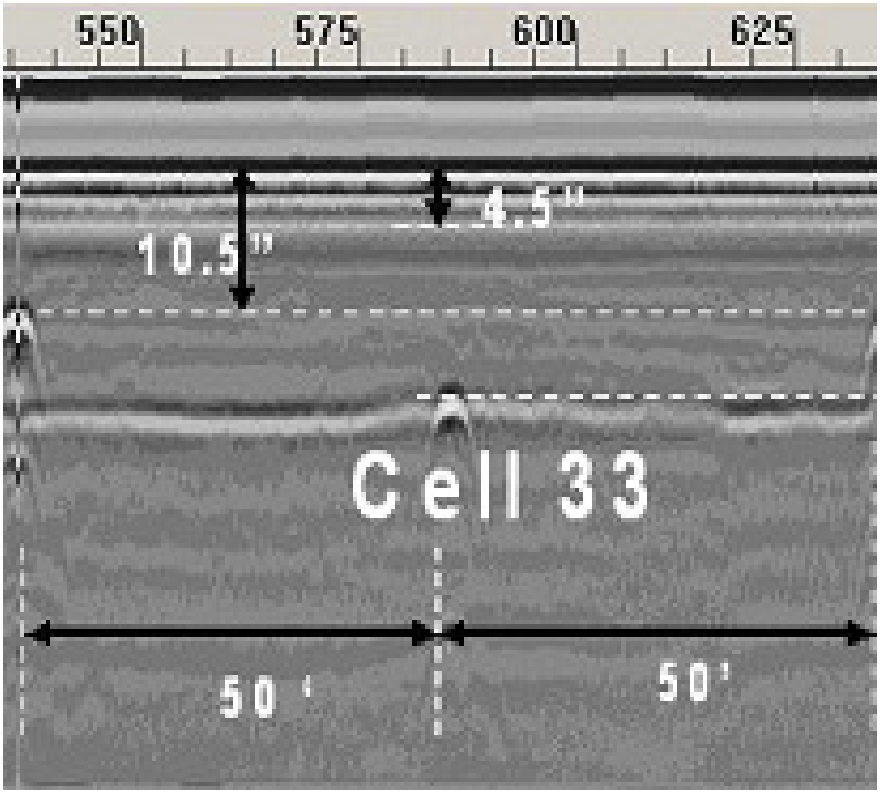

Figure 2.9: GPR image from metal plates.

Chapter 3

Potentials of the Layered Electromagnetic Green's Functions

In Chapter 1, several drawbacks of the traditional GPR technique resulting a non-rigorous back-analysis of the GPR measurement are discussed. In order to improve the GPR technique comprehensively, however, the drawbacks can be fixed by investigating into a more rigorous model of the electromagnetic wave propagation in a layered system. By solving the Maxwells equations in a layered medium, a complete set of 3D layered electromagnetic (EM) Green's functions is derived using the integral transform method by way of transverse electric and

transverse magnetic scalar potentials, featuring a new direct formulation for the field forms of the EM Green's functions (in spatial domain), as will be illustrated in this chapter.

In computational electromagnetism, an approach toward evaluating the EM field via the method of moments (MOM) has been widely used in conjunction with both electric/magnetic field integral equation (EFIE/MFIE) methods [11, 12] and mixed-potential integral equation (MPIE) theories [13, 14, 15, 16]. Because the potential forms of the spectral Green's functions are less singular than the corresponding field forms, the Sommerfeld integrals featured by MPIE converge faster than those present in EFIE/MFIE. However, as first pointed out by Sommerfeld [17], in order to satisfy the interfacial conditions in a layered medium, the vector potential $\mathbf{A}$ used by MPIE due to vertical current source (perpendicular to the interfaces) must be different from that due to a horizontal current source. Thus, a choice has to be made for the dyadic Green's function between the Sommerfeld potential and the transverse potential [13, 18]. To remedy the problem, the use of transverse electric/magnetic (TE/TM) scalar potentials can provide the complete solution for a layered medium without strolling between these two types of dyadic Green's functions [19].

In general, evaluation of the relevant improper integrals that is necessary to compute the spatial Green's functions in a layered medium is complicated by two

key impediments: a) the slow convergence of the spectral Green's functions caused by insufficient integrand decay, especially when the source and receiver are close to each other, and b) highly oscillating Hankel transform kernel $J_\nu(x)$ for large radial distances x. In this setting, extensive research has been performed to expedite the computation of the spatial Green's functions in a layered medium, see e.g. [20, 18, 21]. In particular, an asymptotic extraction for the spectral Green's functions [22] has been shown to result in significant reduction of the computation time necessary to evaluate the potential forms of the Green's function. To date, however, technical literature has been void of attempts to deploy a similar approach toward the evaluation of the corresponding *field forms*, likely due to the fact that the field forms of the spectral Green's functions exhibit higher singularity (as the receiver approaches the source) than their potential-form counterparts.

To help bridge the gap, a pair of scalar TE/TM potentials are first introduced to represent the spectral Green's functions for a layered medium. On employing the Hankel integral transform and Fourier series expansion to uncouple the Maxwell's equations in the spectral domain, the field forms of the Green's functions in the spatial domain are shown to permit a unified integral representation involving the spectral TE/TM potentials. For a rigorous and systematic treatment of the featured improper integrals, the latter are evaluated via the method of asymptotic decomposition where the leading asymptotic expansions of germane

kernels are extracted and integrated analytically, so that the remaining parts with strong decay can be evaluated numerically. This scheme is particularly useful when computing the near-field EM response, where the spectral Green's functions decay at unacceptably slow rate with increasing values of the transform parameter. In such situations the extracted asymptotic behavior completely captures the singularities of the spectral Green's function, causing the residual kernel to decay fast and, upon integration, to bear no additional singularities of the spatial EM solution. The above developments are reinforced through the use of contour numerical integration and self-adaptive quadrature scheme to evaluate the residual components, with the benefit of added robustness in dealing with multiple surface- and interface-wave poles along the formal path of integration and decreased sensitivity to the radial (source-receiver) distance. Through the proposed developments, it is in particular shown that the computational effort required to evaluate the *field forms* of the spatial Green's functions is commensurate to (and in fact not more involved than) that affiliated with the respective *potential forms*.

3.1 Method of scalar potentials

For a time-harmonic EM field with implicit time dependence $e^{-i\omega t}$, the Maxwell's equations in a homogeneous, isotropic medium can be written as

$$\begin{aligned} \nabla \cdot \mathbf{E} &= \varrho/\epsilon, \quad \nabla \times \mathbf{E} = i\omega \mathbf{B}, \\ \nabla \cdot \mathbf{B} &= 0, \qquad \nabla \times \mathbf{B} = \mu\, \mathbf{J} - i\omega\mu\epsilon \mathbf{E}, \end{aligned} \tag{3.1}$$

where $i = \sqrt{-1}$; $\mathbf{E}$ and $\mathbf{B}$ are respectively the electric and magnetic flux field; μ denotes permeability; $\mathbf{J}$ is the current density; ϱ is the charge density; ω stands for angular frequency, and ϵ denotes the complex-valued permittivity given by

$$\epsilon = \varepsilon + i\sigma/\omega, \quad \sigma \geqslant 0, \tag{3.2}$$

where σ signifies the conductivity of the medium, and ε is the permittivity [23]. On the basis of (3.1), $\mathbf{E}$ and $\mathbf{B}$ vector fields can be shown to admit potential representation

$$\begin{aligned} \mathbf{E} &= i\omega(\nabla \times \phi_1 \hat{e}_z + \nabla\nabla \cdot \phi_2 \hat{e}_z + k^2 \phi_2 \hat{e}_z), \\ \mathbf{B} &= \nabla\nabla \cdot \phi_1 \hat{e}_z + k^2 \phi_1 \hat{e}_z + k^2 \nabla \times \phi_2 \hat{e}_z, \end{aligned} \tag{3.3}$$

in a cylindrical coordinate system (ρ, θ, z), where $\hat{e}_z$ is the unit vector in the z-direction, $k = \omega\sqrt{\mu\,\epsilon}$ denotes the wave number [19]. Here ϕ_1 and ϕ_2 are termed the scalar TE and TM potentials, as they relate respectively to the transverse electric and transverse magnetic components of the EM field. In a region free of

currents and charges, each ϕ_1 and ϕ_2 satisfy homogeneous Helmholtz equation, namely

$$(\nabla^2 + k^2)\phi_q = 0, \qquad q = 1, 2. \tag{3.4}$$

For the solution of (3.4), it is instructive to expand the azimuthal dependence of the TE/TM potentials in Fourier series as

$$\phi_q(\rho, \theta, z) = \sum_{m=-\infty}^{\infty} \phi_{q_m}(\rho, z) e^{im\theta}, \qquad q = 1, 2. \tag{3.5}$$

In this setting, the radial variation of ϕ_{q_m} can be conveniently decomposed via the m^{th}-order Hankel transform pair

$$\begin{aligned} \widetilde{\phi_{q_m}}^m(\xi, z) &= \int_0^\infty \phi_{q_m}(\rho, z) \rho J_m(\rho\xi) d\rho, \\ \phi_{q_m}(\rho, z) &= \int_0^\infty \widetilde{\phi_{q_m}}^m(\xi, z) \xi J_m(\rho\xi) d\xi, \end{aligned} \tag{3.6}$$

which, on denoting $(\cdot)' = \partial(\cdot)/\partial z$, reduces (3.4) to

$$\left(\widetilde{\phi_{q_m}}^m\right)'' + (k^2 - \xi^2)\widetilde{\phi_{q_m}}^m = 0, \qquad q = 1, 2. \tag{3.7}$$

The general solution of (3.7) can be represented as the sum of up- and down-going waves in the z-direction as

$$\widetilde{\phi_{q_m}}^m = A_{q_m}(\xi) e^{\gamma z} + B_{q_m}(\xi) e^{-\gamma z}, \tag{3.8}$$

where $\gamma = \sqrt{\xi^2 - k^2}$, and A_{q_m} and B_{q_m} are constants of integration to be determined from the interfacial, boundary, and radiation conditions. Following [11], let

$\xi = \xi_r + i\xi_i$ and $k = k_r + ik_i$ where $\gamma = \sqrt{(\xi_r^2 - \xi_i^2 - k_r^2 + k_i^2) + 2i(\xi_r\xi_i - k_r k_i)}$. In this setting, γ can be rendered single-valued by taking the branch cuts emanating from $\pm k$ as curves where $\mathrm{Re}(\gamma) = 0$, namely

$$\xi_r\xi_i = k_r k_i, \qquad \xi_r^2 - \xi_i^2 < k_r^2 - k_i^2$$

as shown in Fig. 3.1.

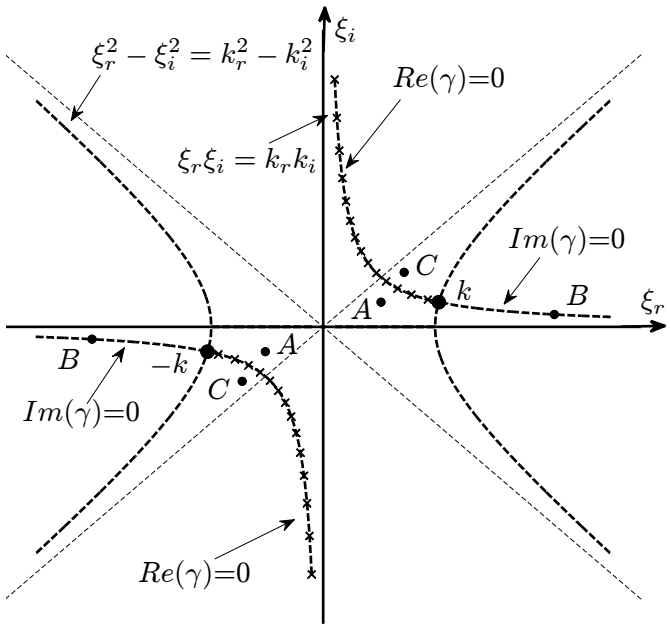

Figure 3.1: Choice of branch cuts.

For further reference it is noted that the field-potential relationships (3.3), on transformation into the spectral domain, can be rearranged to read

$$\widetilde{E_{\rho_m}}^{m+1} \pm i\widetilde{E_{\theta_m}}^{m+1} = i\omega\xi\big[i\widetilde{\phi_{1_m}}^{m} \mp \big(\widetilde{\phi_{2_m}}^{m}\big)'\big], \tag{3.9}$$

$$\widetilde{E_{z_m}}^{m} = i\omega\xi^2\widetilde{\phi_{2_m}}^{m},$$

in terms of the **E** field, and

$$\widetilde{B_{\rho_m}}^{m+1} \pm i\widetilde{B_{\theta_m}}^{m+1} = \xi\big[\mp\big(\widetilde{\phi_{1_m}}^{m}\big)' + ik^2\widetilde{\phi_{2_m}}^{m}\big], \tag{3.10}$$

$$\widetilde{B_{z_m}}^{m} = \xi^2\widetilde{\phi_{1_m}}^{m},$$

in terms of the **B** field. To handle (3.9) and (3.10) in a compact manner, it is convenient to introduce an auxiliary set of scalar fields, $u_{p_m}(\xi, z)$ and $v_{p_m}(\xi, z)$ $(p = 1, 2, 3)$, such that

$$\begin{aligned}
2u_{p_m} &= \big(\widetilde{E_{\rho_m}}^{m+1} + i\widetilde{E_{\theta_m}}^{m+1}\big) \pm \big(\widetilde{E_{\rho_m}}^{m-1} - i\widetilde{E_{\theta_m}}^{m-1}\big), \\
2v_{p_m} &= \big(\widetilde{B_{\rho_m}}^{m+1} + i\widetilde{B_{\theta_m}}^{m+1}\big) \pm \big(\widetilde{B_{\rho_m}}^{m-1} - i\widetilde{B_{\theta_m}}^{m-1}\big), \\
&\text{for} \quad p \neq 2, \qquad u_{2_m} = \widetilde{E_{z_m}}^{m}, \quad v_{2_m} = \widetilde{B_{z_m}}^{m},
\end{aligned} \tag{3.11}$$

where the "+" sign applies for $p=1$, while the "−" sign is assumed when $p=3$. As will be shown later, (3.11) are useful toward uncoupling the transformed solution into the TE- and TM-mode waves.

3.2 Wave propagation in a layered medium

Consider a stratified medium with n homogeneous isotropic layers between two half-spaces as shown in Fig. 3.2. For convenience, the origin of the cylindrical coordinate system is set at the top interface, with the positive z-direction (perpendicular to layer interfaces) pointing down. By labeling the layer interfaces

from 0 to $n+1$, the j^{th} domain ($j = 0, 1, \cdots n+1$), hereon denoted as $\mathcal{L}_j$, has properties ϵ_j, μ_j and σ_j, and thickness $h_j = z_j - z_{j-1}$, where z_j represents the bottom of the j^{th} layer. Here it is noted that the foregoing definition makes use of two auxiliary elevations, $z_{-1} < 0$ and $z_{n+1} > z_n$, which are to be interpreted simply as reference depths (in the respective half-spaces) and *not* as physical layer interfaces *nor* domain boundaries.

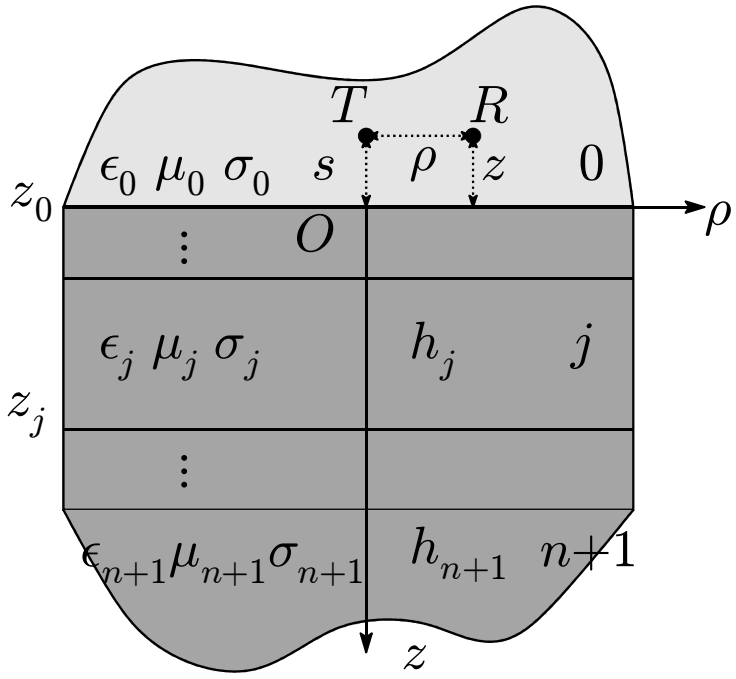

Figure 3.2: Schematics of the layered system.

In the context of (3.4) which precludes the source terms from the field equation, the action of a point source at an arbitrary depth $z_{\ell-1} < s < z_\ell$ within domain $\mathcal{L}_\ell$ can be conveniently represented as a set of *prescribed discontinuities* in the electric

and magnetic field across plane $z = s$, namely

$$E_\alpha(\rho,\theta,z)\big|_{z=s^-}^{z=s^+} = P_\alpha(\rho,\theta) = \sum_{m=-\infty}^{\infty} P_{\alpha,m}(\rho)\; e^{im\theta},$$
$$B_\alpha(\rho,\theta,z)\big|_{z=s^-}^{z=s^+} = Q_\alpha(\rho,\theta) = \sum_{m=-\infty}^{\infty} Q_{\alpha,m}(\rho)\; e^{im\theta}, \tag{3.12}$$

where $\alpha = \rho, \theta, z$ and $f(z)|_{z=s^-}^{z=s^+} = f(s^+) - f(s^-)$. In this setting, the transformed solution for domain $\mathcal{L}_j$ that accounts for the presence of discontinuities (3.12) can be obtained by endowing (3.8) with depth-independent coefficients $A_{q_m}^{j1}$, $B_{q_m}^{j1}$ $(j = 0, 1, \cdots n+1)$, $A_{q_m}^{\ell 2}$ and $B_{q_m}^{\ell 2}$ such that

$$\begin{aligned} A_{q_m}^{j} &= A_{q_m}^{j1}(\xi) + \delta_{j\ell}\, H(s-z)\, A_{q_m}^{\ell 2}(\xi), \\ B_{q_m}^{j} &= B_{q_m}^{j1}(\xi) + \delta_{j\ell}\, H(z-s)\, B_{q_m}^{\ell 2}(\xi), \end{aligned} \quad q = 1, 2, \tag{3.13}$$

where $H(x)$ is the Heaviside step function, and $\delta_{j\ell}$ denotes the Kronecker delta.

For the robustness of the ensuing analytical and computational treatment, it is next useful to make reference to the following dimensionless parameters

$$\begin{gathered} \bar{\rho} = k_{\rm o}\rho, \quad \bar{z} = k_{\rm o} z, \quad \bar{s} = k_{\rm o} s, \quad \bar{h}_j = k_{\rm o} h_j, \quad \bar{z}_j = k_{\rm o} z_j, \\ \bar{\mu} = \frac{\mu}{\mu_{\rm o}}, \quad \bar{\epsilon} = \frac{\epsilon}{\epsilon_{\rm o}}, \quad \bar{k} = \frac{k}{k_{\rm o}}, \quad \bar{\xi} = \frac{\xi}{k_{\rm o}}, \quad \bar{\gamma} = \frac{\gamma}{k_{\rm o}}, \end{gathered} \tag{3.14}$$

where $k_{\rm o} = \omega\sqrt{\epsilon_{\rm o}\mu_{\rm o}}$ is the reference wave number, while $\epsilon_{\rm o}$ and $\mu_{\rm o}$ are the reference permittivity and permeability, respectively. By way of (3.14), the dimensionless counterpart of (3.11) for domain $\mathcal{L}_j$ can be written as

$$\bar{u}_{p_m}^{j}(\bar{\xi},\bar{z}) = \frac{u_{p_m}^{j}(\xi,z)}{\mathcal{J}_m \omega\mu_{\rm o} k_{\rm o}^3}, \quad \bar{v}_{p_m}^{j}(\bar{\xi},\bar{z}) = \frac{v_{p_m}^{j}(\xi,z)}{\mathcal{J}_m \mu_{\rm o} k_{\rm o}^4}, \tag{3.15}$$

where $p = 1, 2, 3$, and $\mathcal{J}_m$ relates to the m^{th}-order Fourier coefficient of the discontinuities in (3.12) to be specified later. In devising the dimensionless variant of (3.13), on the other hand, it is beneficial to interject suitable exponential terms as

$$\begin{aligned} a^j_{1_m}(\bar{\xi}) &= (\mathcal{J}_m \mu_{\text{o}} k_{\text{o}}^2)^{-1} A^j_{1_m}(\xi)\, e^{\bar{\gamma}_j \bar{z}_j}, \\ b^j_{1_m}(\bar{\xi}) &= (\mathcal{J}_m \mu_{\text{o}} k_{\text{o}}^2)^{-1} B^j_{1_m}(\xi)\, e^{-\bar{\gamma}_j \bar{z}_{j-1}}, \\ a^j_{2_m}(\bar{\xi}) &= (\mathcal{J}_m \mu_{\text{o}} k_{\text{o}})^{-1} A^j_{2_m}(\xi)\, e^{\bar{\gamma}_j \bar{z}_j}, \\ b^j_{2_m}(\bar{\xi}) &= (\mathcal{J}_m \mu_{\text{o}} k_{\text{o}})^{-1} B^j_{2_m}(\xi)\, e^{-\bar{\gamma}_j \bar{z}_{j-1}}, \end{aligned} \tag{3.16}$$

such that, in light of up-and-down wave propagation through the stratified medium, the associated propagator matrices can be rendered finite and numerically stable for large values of $\bar{\xi}$. With such definitions, one in particular finds that

$$\begin{bmatrix} \bar{u}^j_{1_m} \\ \bar{v}^j_{2_m} \\ \bar{v}^j_{3_m} \end{bmatrix} = \begin{bmatrix} -\bar{\xi} & -\bar{\xi} \\ \bar{\xi}^2 & \bar{\xi}^2 \\ -\bar{\xi}\bar{\gamma}_j & \bar{\xi}\bar{\gamma}_j \end{bmatrix} \begin{bmatrix} a^j_{1_m} e^{\bar{\gamma}_j(\bar{z}-\bar{z}_j)} \\ b^j_{1_m} e^{-\bar{\gamma}_j(\bar{z}-\bar{z}_{j-1})} \end{bmatrix}, \tag{3.17}$$

in terms of potential ϕ_1 which synthesizes TE-mode waves, and

$$\begin{bmatrix} \bar{v}^j_{1_m} \\ \bar{u}^j_{2_m} \\ \bar{u}^j_{3_m} \end{bmatrix} = \begin{bmatrix} i\bar{k}_j^2\bar{\xi} & i\bar{k}_j^2\bar{\xi} \\ i\bar{\xi}^2 & i\bar{\xi}^2 \\ -i\bar{\xi}\bar{\gamma}_j & i\bar{\xi}\bar{\gamma}_j \end{bmatrix} \begin{bmatrix} a^j_{2_m} e^{\bar{\gamma}_j(\bar{z}-\bar{z}_j)} \\ b^j_{2_m} e^{-\bar{\gamma}_j(\bar{z}-\bar{z}_{j-1})} \end{bmatrix}, \tag{3.18}$$

in terms of potential ϕ_2 which represents TM-mode waves. Recalling the implicit time factor $e^{-i\omega t}$, one may in particular note that the coefficients $a^j_{q_m}$ $(q = 1, 2)$

can be affiliated with upgoing waves in the j^{th} medium; in contrast, $b^j_{q_m}$ signify the magnitudes of complementary downgoing waves.

With the transformed solution given by (3.17) and (3.18) for domain $\mathcal{L}_j$ ($j = 0, 1, \cdots n+1$) at hand, the next step in obtaining the layered Green's functions entails computation of the featured coefficients of integration from the prescribed interfacial, jump and radiation conditions.

3.2.1 Propagation of TE-mode waves

To compute the solution for $\bar{u}^j_{1_m}$, $\bar{v}^j_{2_m}$ and $\bar{v}^j_{3_m}$ featured in the TE matrix relationship (3.17), the coefficients of integration $a^j_{1_m}$ and $b^j_{1_m}$ can be resolved from: a) the interfacial conditions

$$\begin{aligned} \bar{u}^j_{1_m}(\bar{\xi}, \bar{z}_j) &= \bar{u}^{j+1}_{1_m}(\bar{\xi}, \bar{z}_j), \\ \bar{v}^j_{2_m}(\bar{\xi}, \bar{z}_j) &= \bar{v}^{j+1}_{2_m}(\bar{\xi}, \bar{z}_j), \\ \bar{v}^j_{3_m}(\bar{\xi}, \bar{z}_j)/\bar{\mu}_j &= \bar{v}^{j+1}_{3_m}(\bar{\xi}, \bar{z}_j)/\bar{\mu}_{j+1}, \end{aligned} \tag{3.19}$$

signifying respectively the continuity of the tangential component of $\mathbf{E}$, continuity of the normal component of $\mathbf{B}$, and discontinuity of the tangential component of $\mathbf{B}$ across $\bar{z} = \bar{z}_j$ ($j = 0, 1, \cdots n$); b) the jump conditions

$$\begin{aligned} \bar{u}^\ell_{1_m}(\bar{\xi}, \bar{z})\big|^{\bar{z}=\bar{s}^+}_{\bar{z}=\bar{s}^-} &= 0, \\ \bar{v}^\ell_{2_m}(\bar{\xi}, \bar{z})\big|^{\bar{z}=\bar{s}^+}_{\bar{z}=\bar{s}^-} &= 0, \\ \bar{v}^\ell_{3_m}(\bar{\xi}, \bar{z})\big|^{\bar{z}=\bar{s}^+}_{\bar{z}=\bar{s}^-} &= \tfrac{1}{2}(U^+_m - U^-_m), \end{aligned} \tag{3.20}$$

across the internal source plane $\bar{z} = \bar{s}$ where

$$U_m^{\pm}(\bar{\xi}) \;=\; \widetilde{Q_{\rho,m}}^{m+1}(\bar{\xi}) \,\pm\, i\,\widetilde{Q_{\theta,m}}^{m+1}(\bar{\xi}), \tag{3.21}$$

and c) the radiation condition which precludes the existence of incoming **E** and **B** fields from infinity, namely

$$\begin{aligned} &\lim_{\bar{z}\to-\infty} \bar{u}_{1_m}^0(\bar{\xi},\bar{z}) = 0,\ \lim_{\bar{z}\to\infty} \bar{u}_{1_m}^{n+1}(\bar{\xi},\bar{z}) = 0, \\ &\lim_{\bar{z}\to-\infty} \bar{v}_{p_m}^0(\bar{\xi},\bar{z}) = 0,\ \lim_{\bar{z}\to\infty} \bar{v}_{p_m}^{n+1}(\bar{\xi},\bar{z}) = 0,\ p = 2,3. \end{aligned} \tag{3.22}$$

By means of (3.16) and the TE matrix relationship (3.17), the jump condition (3.20) yields

$$a_{1_m}^{\ell 2}(\bar{\xi}) = s_{1_m}^u e^{-\bar{\gamma}_\ell(\bar{s}-\bar{z}_\ell)},\ b_{1_m}^{\ell 2}(\bar{\xi}) = s_{1_m}^d e^{-\bar{\gamma}_\ell(\bar{z}_{\ell-1}-\bar{s})}, \tag{3.23}$$

where the source coefficients are given by

$$s_{1_m}^u(\bar{\xi}) = s_{1_m}^d(\bar{\xi}) = \frac{U_m^+ - U_m^-}{4\bar{\xi}\bar{\gamma}_\ell}. \tag{3.24}$$

On substituting (3.17) into (3.19) for the j^{th} interface, the relationship between the coefficients of the adjacent layers, $\mathcal{L}_j$ and $\mathcal{L}_{j+1}$, can be formulated by introducing the propagator matrix for TE-mode waves as

$$\begin{bmatrix} a_{1_m}^j \\ b_{1_m}^{j+1} \end{bmatrix} = \begin{bmatrix} T_j^{u,\mathrm{E}} & R_j^{d,\mathrm{E}} \\ R_j^{u,\mathrm{E}} & T_j^{d,\mathrm{E}} \end{bmatrix} \begin{bmatrix} a_{1_m}^{j+1}\mathcal{E}_{j+1} \\ b_{1_m}^j \mathcal{E}_j \end{bmatrix}, \tag{3.25}$$

where superscript "E" refers to the TE mode; $\mathcal{E}_j = e^{-\bar{\gamma}_j \bar{h}_j}$,

$$\begin{aligned} T_j^{u,\mathrm{E}} &= \frac{2\kappa_{j+1}}{\kappa_j + \kappa_{j+1}}, \qquad R_j^{d,\mathrm{E}} = \frac{\kappa_j - \kappa_{j+1}}{\kappa_j + \kappa_{j+1}}, \\ R_j^{u,\mathrm{E}} &= \frac{\kappa_{j+1} - \kappa_j}{\kappa_j + \kappa_{j+1}}, \qquad T_j^{d,\mathrm{E}} = \frac{2\kappa_j}{\kappa_j + \kappa_{j+1}}, \end{aligned} \tag{3.26}$$

and $\kappa_j = \bar{\gamma}_j/\bar{\mu}_j$. In (3.25) and (3.26), $T_j^{u,\mathrm{E}}$ (resp. $R_j^{u,\mathrm{E}}$) may be recognized as the transmission (resp. reflection) coefficient for the upwardly propagating TE-mode wave impinging on the j^{th} interface from $\mathcal{L}_{j+1}$. Similarly, $T_j^{d,\mathrm{E}}$ and $R_j^{d,\mathrm{E}}$ are identified as the corresponding transmission and reflection coefficients for the downwardly propagating TE wave in $\mathcal{L}_j$.

Due to the fact that each interfacial condition affects the neighboring layers only, the overall coefficient matrix for $a_{1_m}^j$ and $b_{1_m}^j$ $(j = 0, 1, \cdots n+1)$ is composed of 2×2 blocks straddling the main diagonal. As a result, any TE-mode disturbance originating at $z = s$ can be propagated via (3.25) from one interface to another, and consequently factorized to compute the unknown coefficients in each layer. This approach can be illustrated by initiating (3.25) from the top interface $\bar{z} = \bar{z}_0$, and noting that $b_{1_m}^0 = 0$ due to radiation condition (3.22) so that

$$\begin{aligned} a_{1_m}^0 &= T_0^{u,\mathrm{E}} a_{1_m}^1 \mathcal{E}_1 = \widehat{T}_0^{u,\mathrm{E}} a_{1_m}^1 \mathcal{E}_1, \\ b_{1_m}^1 &= R_0^{u,\mathrm{E}} a_{1_m}^1 \mathcal{E}_1 = \widehat{R}_0^{u,\mathrm{E}} a_{1_m}^1 \mathcal{E}_1, \end{aligned} \tag{3.27}$$

where $\widehat{T}_0^{u,\mathrm{E}}$ and $\widehat{R}_0^{u,\mathrm{E}}$ are the *generalized* TE-mode transmission and reflection coefficients which include all multiple reflections and transmissions above $\bar{z} = \bar{z}_0$ (in this case none). Continuing along the same line, it can be shown by enforcing (3.25) at the next interface $\bar{z} = \bar{z}_1$ and making use of second of (3.27), that the

coefficients in $\mathcal{L}_2$ are related to those in $\mathcal{L}_1$ as

$$a^1_{1_m} = \widehat{T}^{u,\mathrm{E}}_1 a^2_{1_m}\mathcal{E}_2, \qquad b^2_{1_m} = \widehat{R}^{u,\mathrm{E}}_1 a^2_{1_m}\mathcal{E}_2, \tag{3.28}$$

where

$$\widehat{T}^{u,\mathrm{E}}_1 = (1 - R^{d,\mathrm{E}}_1 \widehat{R}^{u,\mathrm{E}}_0 \mathcal{E}_1^2)^{-1}\ T^{u,\mathrm{E}}_1,$$
$$\widehat{R}^{u,\mathrm{E}}_1 = R^{u,\mathrm{E}}_1 + T^{d,\mathrm{E}}_1 \widehat{R}^{u,\mathrm{E}}_0 \widehat{T}^{u,\mathrm{E}}_1 \mathcal{E}_1^2.$$

Continuing the process recursively until $\bar{z} = \bar{z}_{\ell-2}$, one finds that

$$a^j_{1_m} = \widehat{T}^{u,\mathrm{E}}_j a^{j+1}_{1_m}\mathcal{E}_{j+1} = \big(\widehat{T}^{u,\mathrm{E}}_j \mathcal{E}_{j+1}\big)\cdots\big(\widehat{T}^{u,\mathrm{E}}_{\ell-1}\mathcal{E}_\ell\big)a^\ell_{1_m},$$
$$b^j_{1_m} = \big(\widehat{R}^{u,\mathrm{E}}_{j-1}\mathcal{E}_j\big)a^j_{1_m}, \tag{3.29}$$

where $j = 0, 1, \cdots, \ell-1$, and

$$\widehat{T}^{u,\mathrm{E}}_j = (1 - R^{d,\mathrm{E}}_j \widehat{R}^{u,\mathrm{E}}_{j-1} \mathcal{E}_j^2)^{-1}\ T^{u,\mathrm{E}}_j,$$
$$\widehat{R}^{u,\mathrm{E}}_j = R^{u,\mathrm{E}}_j + T^{d,\mathrm{E}}_j \widehat{R}^{u,\mathrm{E}}_{j-1} \widehat{T}^{u,\mathrm{E}}_j \mathcal{E}_j^2, \tag{3.30}$$

together with the reflection formula at $\bar{z} = \bar{z}_{\ell-1}$, namely

$$b^\ell_{1_m} = \big(\widehat{R}^{u,\mathrm{E}}_{\ell-1}\mathcal{E}_\ell\big)a^\ell_{1_m}. \tag{3.31}$$

Here it is emphasized that $T^{u,\mathrm{E}}_j$, $R^{u,\mathrm{E}}_j$, $T^{d,\mathrm{E}}_j$ and $R^{d,\mathrm{E}}_j$ are affiliated with the j^{th} interface only; in contrast, the *generalized* transmission and reflection coefficients $\widehat{T}^{u,\mathrm{E}}_j$, $\widehat{R}^{u,\mathrm{E}}_j$, $\widehat{T}^{d,\mathrm{E}}_j$ and $\widehat{R}^{d,\mathrm{E}}_j$ synthesize all multiple reflections and transmissions of the TE waves *at and above* the j^{th} interface ($j<\ell$).

In a similar fashion, the coefficients in the layers below the source can be factorized as

$$\begin{aligned} b^j_{1_m} &= \big(\widehat{T}^{d,\mathrm{E}}_{j-1}\mathcal{E}_{j-1}\big)\cdots\big(\widehat{T}^{d,\mathrm{E}}_{\ell}\mathcal{E}_{\ell}\big)b^{\ell}_{1_m}, \\ a^j_{1_m} &= \big(\widehat{R}^{d,\mathrm{E}}_{j}\mathcal{E}_{j}\big)b^{j}_{1_m}, \end{aligned} \tag{3.32}$$

where $j = \ell+1, \ell+2, \cdots, n+1$, and

$$\begin{aligned} \widehat{T}^{d,\mathrm{E}}_{j} &= (1 - R^{u,\mathrm{E}}_{j}\widehat{R}^{d,\mathrm{E}}_{j+1}\mathcal{E}^2_{j+1})^{-1}\ T^{d,\mathrm{E}}_{j}, \\ \widehat{R}^{d,\mathrm{E}}_{j} &= R^{d,\mathrm{E}}_{j} + T^{u,\mathrm{E}}_{j}\widehat{R}^{d,\mathrm{E}}_{j+1}\widehat{T}^{d,\mathrm{E}}_{j}\mathcal{E}^2_{j+1}; \end{aligned} \tag{3.33}$$

a result that is accompanied by the reflection formula for the ℓ^{th} interface

$$a^{\ell}_{1_m} = \big(\widehat{R}^{d,\mathrm{E}}_{\ell}\mathcal{E}_{\ell}\big)b^{\ell}_{1_m}. \tag{3.34}$$

Note that the generalized transmission and reflection coefficients in (3.32)–(3.34), indicated by the hat symbol, encompass all multiple reflections and transmissions *at and below* the j^{th} interface ($j > \ell$).

From (3.29) and (3.32), one finds that the solution in the layered medium "propagates" outward from $\mathcal{L}_\ell$ toward any given layer, thus allowing $a^j_{1_m}$ and $b^j_{1_m}$ ($j \neq \ell$) to be expressed in terms of $a^{\ell}_{1_m}$ and $b^{\ell}_{1_m}$.

On substituting (3.16) into (3.31) and (3.34), and recalling from (3.13) that the particular solution in the ℓ^{th} layer, given by $a^{\ell,2}_{1_m}$ and $b^{\ell,2}_{1_m}$, vanishes respectively below and above the source, the homogeneous solution in the ℓ^{th} layer can be

computed as

$$\begin{aligned} a_{1_m}^{\ell,1} &= \mathcal{P}_{\mathrm{E}}^{-1}(\widehat{R}_{\ell}^{d,\mathrm{E}}\widehat{R}_{\ell-1}^{u,\mathrm{E}}a_{1_m}^{\ell,2}\mathcal{E}_{\ell}^{2} + \widehat{R}_{\ell}^{d,\mathrm{E}}b_{1_m}^{\ell,2}\mathcal{E}_{\ell}), \\ b_{1_m}^{\ell,1} &= \mathcal{P}_{\mathrm{E}}^{-1}(\widehat{R}_{\ell-1}^{u,\mathrm{E}}\widehat{R}_{\ell}^{d,\mathrm{E}}b_{1_m}^{\ell,2}\mathcal{E}_{\ell}^{2} + \widehat{R}_{\ell-1}^{u,\mathrm{E}}a_{1_m}^{\ell,2}\mathcal{E}_{\ell}), \end{aligned} \tag{3.35}$$

where $\mathcal{P}_{\mathrm{E}} = 1 - \widehat{R}_{\ell-1}^{u,\mathrm{E}}\widehat{R}_{\ell}^{d,\mathrm{E}}\mathcal{E}_{\ell}^{2}$. By virtue of (3.16), (3.23), and (3.24), on the other hand, the corresponding particular solution can be shown to read

$$a_{1_m}^{\ell} = \mathcal{K}^{u,\mathrm{E}}\,\frac{U_m^{+} - U_m^{-}}{4\bar{\xi}\bar{\gamma}_{\ell}}, \qquad b_{1_m}^{\ell} = \mathcal{K}^{d,\mathrm{E}}\,\frac{U_m^{+} - U_m^{-}}{4\bar{\xi}\bar{\gamma}_{\ell}}, \tag{3.36}$$

where $\mathcal{K}^{u,\mathrm{E}}$ and $\mathcal{K}^{d,\mathrm{E}}$ are given as

$$\begin{aligned} \mathcal{K}^{u,\mathrm{E}} &= H(\bar{s}-\bar{z})e^{-\bar{\gamma}_{\ell}(\bar{s}-\bar{z}_{\ell})} + \mathcal{P}_{\mathrm{E}}^{-1}\widehat{R}_{\ell}^{d,\mathrm{E}}\mathcal{E}_{\ell}\Big(\widehat{R}_{\ell-1}^{u,\mathrm{E}}e^{-\bar{\gamma}_{\ell}(\bar{s}-\bar{z}_{\ell})}\mathcal{E}_{\ell} + e^{-\bar{\gamma}_{\ell}(\bar{z}_{\ell-1}-\bar{s})}\Big), \\ \mathcal{K}^{d,\mathrm{E}} &= H(\bar{z}-\bar{s})e^{-\bar{\gamma}_{\ell}(\bar{z}_{\ell-1}-\bar{s})} + \mathcal{P}_{\mathrm{E}}^{-1}\widehat{R}_{\ell-1}^{u,\mathrm{E}}\mathcal{E}_{\ell}\Big(\widehat{R}_{\ell}^{d,\mathrm{E}}e^{-\bar{\gamma}_{\ell}(\bar{z}_{\ell-1}-\bar{s})}\mathcal{E}_{\ell} + e^{-\bar{\gamma}_{\ell}(\bar{s}-\bar{z}_{\ell})}\Big). \end{aligned}$$

.

A substitution of (3.36) into the TE matrix relationship (3.17) yields

$$\begin{aligned} \bar{u}_{1_m}^{\ell} &= \big[\mathcal{K}^{u,\mathrm{E}}e^{\bar{\gamma}_{\ell}(\bar{z}-\bar{z}_{\ell})} + \mathcal{K}^{d,\mathrm{E}}e^{\bar{\gamma}_{\ell}(\bar{z}_{\ell-1}-\bar{z})}\big]\frac{(U_m^{-} - U_m^{+})}{4\bar{\gamma}_{\ell}}, \\ \bar{v}_{2_m}^{\ell} &= \big[\mathcal{K}^{u,\mathrm{E}}e^{\bar{\gamma}_{\ell}(\bar{z}-\bar{z}_{\ell})} + \mathcal{K}^{d,\mathrm{E}}e^{\bar{\gamma}_{\ell}(\bar{z}_{\ell-1}-\bar{z})}\big]\frac{\bar{\xi}(U_m^{+} - U_m^{-})}{4\bar{\gamma}_{\ell}}, \\ \bar{v}_{3_m}^{\ell} &= \big[\mathcal{K}^{u,\mathrm{E}}e^{\bar{\gamma}_{\ell}(\bar{z}-\bar{z}_{\ell})} - \mathcal{K}^{d,\mathrm{E}}e^{\bar{\gamma}_{\ell}(\bar{z}_{\ell-1}-\bar{z})}\big]\frac{(U_m^{-} - U_m^{+})}{4}. \end{aligned} \tag{3.37}$$

The above formulation demonstrates that a complete solution for the spectral TE-mode waves in a layered system is synthesized via recursive relations (3.29) and (3.32), together with the source-layer solution (3.36). Once the spectral **E** and **B** Green's functions are computed, the spatial Green's functions can be obtained by way of inverse Hankel transform (3.6).

3.2.2 Propagation of TM-mode waves

Following the solution methodology developed for the TE-mode waves, the coefficients of integration $a^j_{2_m}$ and $b^j_{2_m}$ featured in the TM matrix relationship (3.18) are resolved from: a) the interfacial conditions

$$\begin{aligned} \bar{v}^j_{1_m}(\bar{\xi},\bar{z}_j)/\bar{\mu}_j &= \bar{v}^{j+1}_{1_m}(\bar{\xi},\bar{z}_j)/\bar{\mu}_{j+1}, \\ \bar{\epsilon}_j\bar{u}^j_{2_m}(\bar{\xi},\bar{z}_j) &= \bar{\epsilon}_{j+1}\bar{u}^{j+1}_{2_m}(\bar{\xi},\bar{z}_j), \\ \bar{u}^j_{3_m}(\bar{\xi},\bar{z}_j) &= \bar{u}^{j+1}_{3_m}(\bar{\xi},\bar{z}_j), \end{aligned} \tag{3.38}$$

signifying respectively the discontinuity of the tangential component of $\mathbf{B}$, discontinuity of the normal component of $\mathbf{E}$, and continuity of the tangential component of $\mathbf{E}$; b) the jump conditions

$$\begin{aligned} \bar{v}^\ell_{1_m}(\bar{\xi},\bar{z})\big|^{\bar{z}=\bar{s}^+}_{\bar{z}=\bar{s}^-} &= \tfrac{1}{2}(U^+_m + U^-_m), \\ \bar{u}^\ell_{2_m}(\bar{\xi},\bar{z})\big|^{\bar{z}=\bar{s}^+}_{\bar{z}=\bar{s}^-} &= \tfrac{1}{2}Y_m\cdot\bar{\xi}/\bar{k}^2_\ell, \\ \bar{u}^\ell_{3_m}(\bar{\xi},\bar{z})\big|^{\bar{z}=\bar{s}^+}_{\bar{z}=\bar{s}^-} &= \tfrac{1}{2}(X^+_m - X^-_m)\cdot\bar{\xi}/\bar{k}^2_\ell, \end{aligned} \tag{3.39}$$

across the internal source plane $\bar{z}=\bar{s}$ where

$$\begin{aligned} X^\pm_m(\bar{\xi}) &= \big(\widetilde{P_{\rho,m}}^{\,m+1}(\bar{\xi}) \pm i\widetilde{P_{\theta,m}}^{\,m+1}(\bar{\xi})\big)\cdot\bar{k}^2_\ell/\bar{\xi}, \\ Y_m(\bar{\xi}) &= 2\widetilde{P_{z,m}}^{\,m}(\bar{\xi})\cdot\bar{k}^2_\ell/\bar{\xi}, \end{aligned} \tag{3.40}$$

and c) the radiation conditions

$$\begin{aligned} &\lim_{\bar{z}\to-\infty}\bar{v}^0_{1_m}(\bar{\xi},\bar{z})=0, \quad \lim_{\bar{z}\to\infty}\bar{v}^{n+1}_{1_m}(\bar{\xi},\bar{z})=0, \\ &\lim_{\bar{z}\to-\infty}\bar{u}^0_{p_m}(\bar{\xi},\bar{z})=0, \quad \lim_{\bar{z}\to\infty}\bar{u}^{n+1}_{p_m}(\bar{\xi},\bar{z})=0, \quad p=2,3, \end{aligned} \tag{3.41}$$

By means of (3.16) and the TM matrix relationship (3.18), the jump condition (3.39) requires that

$$a_{2_m}^{\ell 2}(\bar{\xi}) = s_{2_m}^{u} e^{-\bar{\gamma}_\ell(\bar{s}-\bar{z}_\ell)},\ b_{2_m}^{\ell 2}(\bar{\xi}) = s_{2_m}^{d} e^{-\bar{\gamma}_\ell(\bar{z}_{\ell-1}-\bar{s})}, \tag{3.42}$$

where the source coefficients are given by

$$\begin{aligned} s_{2_m}^{u}(\bar{\xi}) &= \frac{X_m^+ - X_m^-}{4i\bar{k}_\ell^2\bar{\gamma}_\ell} - \frac{Y_m}{4i\bar{\xi}\bar{k}_\ell^2}, \\ s_{2_m}^{d}(\bar{\xi}) &= \frac{X_m^+ - X_m^-}{4i\bar{k}_\ell^2\bar{\gamma}_\ell} + \frac{Y_m}{4i\bar{\xi}\bar{k}_\ell^2}. \end{aligned} \tag{3.43}$$

Similarly, the propagator matrix for TM-mode waves can be obtained as

$$\begin{bmatrix} a_{2_m}^{j} \\ \\ b_{2_m}^{j+1} \end{bmatrix} = \begin{bmatrix} T_j^{u,\mathrm{M}} & R_j^{d,\mathrm{M}} \\ \\ R_j^{u,\mathrm{M}} & T_j^{d,\mathrm{M}} \end{bmatrix} \begin{bmatrix} a_{2_m}^{j+1}\mathcal{E}_{j+1} \\ \\ b_{2_m}^{j}\mathcal{E}_j \end{bmatrix}, \tag{3.44}$$

where superscript "M" refers to the TM mode; $\mathcal{E}_j = e^{-\bar{\gamma}_j\bar{h}_j}$,

$$\begin{aligned} T_j^{u,\mathrm{M}} &= \frac{\bar{\epsilon}_{j+1}}{\bar{\epsilon}_j}\frac{2\chi_{j+1}}{\chi_j+\chi_{j+1}}, \quad R_j^{d,\mathrm{M}} = \frac{\chi_j-\chi_{j+1}}{\chi_j+\chi_{j+1}}, \\ R_j^{u,\mathrm{M}} &= \frac{\chi_{j+1}-\chi_j}{\chi_j+\chi_{j+1}}, \qquad T_j^{d,\mathrm{M}} = \frac{\bar{\epsilon}_j}{\bar{\epsilon}_{j+1}}\frac{2\chi_j}{\chi_j+\chi_{j+1}}, \end{aligned} \tag{3.45}$$

and $\chi_j = \bar{\gamma}_j/\bar{\epsilon}_j$. Here $T_j^{u,\mathrm{M}}$ (resp. $R_j^{u,\mathrm{M}}$) is the transmission (resp. reflection) coefficient for the upwardly propagating TM-mode wave impinging on the j^{th} interface from $\mathcal{L}_{j+1}$. Similarly, $T_j^{d,\mathrm{M}}$ and $R_j^{d,\mathrm{M}}$ are the corresponding transmission and reflection coefficients for the TE wave downwardly propagating through $\mathcal{L}_j$.

Owing to the equivalence in form between the TE and TM formulations, the latter solution can be obtained simply by replacing the superscript $\mathrm{E} \to \mathrm{M}$ in

(3.29)–(3.35). The TM counterpart of (3.36), on the other hand, can be obtained by way of (3.16), (3.42) and (3.43) as

$$\begin{aligned} a^{\ell}_{2_m} &= \mathcal{K}_1^{u,\mathrm{M}} \frac{X_m^+ - X_m^-}{4i\bar{k}_\ell^2 \bar{\gamma}_\ell} + \mathcal{K}_2^{u,\mathrm{M}} \frac{Y_m}{4i\bar{\xi}\bar{k}_\ell^2}, \\ b^{\ell}_{2_m} &= \mathcal{K}_1^{d,\mathrm{M}} \frac{X_m^+ - X_m^-}{4i\bar{k}_\ell^2 \bar{\gamma}_\ell} + \mathcal{K}_2^{d,\mathrm{M}} \frac{Y_m}{4i\bar{\xi}\bar{k}_\ell^2}, \end{aligned} \tag{3.46}$$

where the expressions for $\mathcal{K}^{u,\mathrm{M}}$ and $\mathcal{K}^{d,\mathrm{M}}$ are given as

$$\begin{aligned} \mathcal{K}_1^{u,\mathrm{M}} &= H(\bar{s}-\bar{z})e^{-\bar{\gamma}_\ell(\bar{s}-\bar{z}_\ell)} + \ \mathcal{P}_{\mathrm{M}}^{-1}\widehat{R}_\ell^{d,\mathrm{M}}\mathcal{E}_\ell\Big(\widehat{R}_{\ell-1}^{u,\mathrm{M}}e^{-\bar{\gamma}_\ell(\bar{s}-\bar{z}_\ell)}\mathcal{E}_\ell + e^{-\bar{\gamma}_\ell(\bar{z}_{\ell-1}-\bar{s})}\Big), \\ \mathcal{K}_2^{u,\mathrm{M}} &= -H(\bar{s}-\bar{z})e^{-\bar{\gamma}_\ell(\bar{s}-\bar{z}_\ell)} - \ \mathcal{P}_{\mathrm{M}}^{-1}\widehat{R}_\ell^{d,\mathrm{M}}\mathcal{E}_\ell\Big(\widehat{R}_{\ell-1}^{u,\mathrm{M}}e^{-\bar{\gamma}_\ell(\bar{s}-\bar{z}_\ell)}\mathcal{E}_\ell - e^{-\bar{\gamma}_\ell(\bar{z}_{\ell-1}-\bar{s})}\Big), \\ \mathcal{K}_1^{d,\mathrm{M}} &= H(\bar{z}-\bar{s})e^{-\bar{\gamma}_\ell(\bar{z}_{\ell-1}-\bar{s})} + \ \mathcal{P}_{\mathrm{M}}^{-1}\widehat{R}_{\ell-1}^{u,\mathrm{M}}\mathcal{E}_\ell\Big(\widehat{R}_\ell^{d,\mathrm{M}}e^{-\bar{\gamma}_\ell(\bar{z}_{\ell-1}-\bar{s})}\mathcal{E}_\ell + e^{-\bar{\gamma}_\ell(\bar{s}-\bar{z}_\ell)}\Big), \\ \mathcal{K}_2^{d,\mathrm{M}} &= H(\bar{z}-\bar{s})e^{-\bar{\gamma}_\ell(\bar{z}_{\ell-1}-\bar{s})} + \ \mathcal{P}_{\mathrm{M}}^{-1}\widehat{R}_{\ell-1}^{u,\mathrm{M}}\mathcal{E}_\ell\Big(\widehat{R}_\ell^{d,\mathrm{M}}e^{-\bar{\gamma}_\ell(\bar{z}_{\ell-1}-\bar{s})}\mathcal{E}_\ell - e^{-\bar{\gamma}_\ell(\bar{s}-\bar{z}_\ell)}\Big). \end{aligned}$$

On substituting (3.46) into the TM matrix relationship (3.18), one finds

$$\begin{aligned} \bar{v}^{\ell}_{1_m} &= \big[\mathcal{K}_2^{u,\mathrm{M}}e^{\bar{\gamma}_\ell(\bar{z}-\bar{z}_\ell)} + \mathcal{K}_2^{d,\mathrm{M}}e^{\bar{\gamma}_\ell(\bar{z}_{\ell-1}-\bar{z})}\big]\frac{Y_m}{4} \\ &+ \big[\mathcal{K}_1^{u,\mathrm{M}}e^{\bar{\gamma}_\ell(\bar{z}-\bar{z}_\ell)} + \mathcal{K}_1^{d,\mathrm{M}}e^{\bar{\gamma}_\ell(\bar{z}_{\ell-1}-\bar{z})}\big]\frac{\bar{\xi}(X_m^+ - X_m^-)}{4\bar{\gamma}_\ell}, \\ \bar{u}^{\ell}_{2_m} &= \big[\mathcal{K}_2^{u,\mathrm{M}}e^{\bar{\gamma}_\ell(\bar{z}-\bar{z}_\ell)} + \mathcal{K}_2^{d,\mathrm{M}}e^{\bar{\gamma}_\ell(\bar{z}_{\ell-1}-\bar{z})}\big]\frac{Y_m\bar{\xi}}{4\bar{k}_\ell^2} \\ &+ \big[\mathcal{K}_1^{u,\mathrm{M}}e^{\bar{\gamma}_\ell(\bar{z}-\bar{z}_\ell)} + \mathcal{K}_1^{d,\mathrm{M}}e^{\bar{\gamma}_\ell(\bar{z}_{\ell-1}-\bar{z})}\big]\frac{\bar{\xi}^2(X_m^+ - X_m^-)}{4\bar{\gamma}_\ell\bar{k}_\ell^2}, \\ \bar{u}^{\ell}_{3_m} &= \big[-\mathcal{K}_2^{u,\mathrm{M}}e^{\bar{\gamma}_\ell(\bar{z}-\bar{z}_\ell)} + \mathcal{K}_2^{d,\mathrm{M}}e^{\bar{\gamma}_\ell(\bar{z}_{\ell-1}-\bar{z})}\big]\frac{\bar{\gamma}_\ell Y_m}{4\bar{k}_\ell^2} \\ &+ \big[\mathcal{K}_1^{u,\mathrm{M}}e^{\bar{\gamma}_\ell(\bar{z}-\bar{z}_\ell)} - \mathcal{K}_1^{d,\mathrm{M}}e^{\bar{\gamma}_\ell(\bar{z}_{\ell-1}-\bar{z})}\big]\frac{(X_m^- - X_m^+)\bar{\xi}}{4\bar{k}_\ell^2}. \end{aligned} \tag{3.47}$$

3.3 Electric Dipole Radiation

So far, the spectral solution has been formulated for an arbitrary source distribution across plane $z = s$ in a layered medium. To obtain the Green's function due to an electric dipole, it is useful to express the horizontal (*i.e.* transverse) and vertical (*i.e.* longitudinal) *point-current* sources in the reference (cylindrical) coordinate system (ρ, θ, z) as

$$\begin{aligned} \mathbf{J}_h^{\,\mathrm{pt}}(\rho,\theta,z) &= \frac{\mathcal{J}_h}{2\pi\rho}\,\delta(\rho)\,\delta(z-s)\,\hat{\mathbf{e}}_h, \\ \mathbf{J}_z^{\,\mathrm{pt}}(\rho,\theta,z) &= \frac{\mathcal{J}_z}{2\pi\rho}\,\delta(\rho)\,\delta(z-s)\,\hat{\mathbf{e}}_z, \end{aligned} \tag{3.48}$$

where $\mathcal{J}_h$ and $\mathcal{J}_z$ signify the respective source amplitudes; $\hat{\mathbf{e}}_z$ is the unit vector in the $z-$direction, and $\hat{\mathbf{e}}_h$ is the unit horizontal vector in the $\theta = \theta_0$ direction given by

$$\hat{\mathbf{e}}_h = \cos(\theta-\theta_0)\,\hat{\mathbf{e}}_\rho - \sin(\theta-\theta_0)\,\hat{\mathbf{e}}_\theta. \tag{3.49}$$

Clearly, the horizontal current density $\mathbf{J}_h^{\,\mathrm{pt}}$ can be described as a discontinuity in the tangential component of the $\mathbf{B}$ field across $z = s$. To represent the action of $\mathbf{J}_z^{\,\mathrm{pt}}$, on the other hand, one may employ the relationship between the electric current density and equivalent magnetic current density

$$\mathbf{M} = \frac{\nabla \times \mathbf{J}}{i\omega\epsilon}, \tag{3.50}$$

which, within the source plane, translates $\mathbf{J}_z^{\,\mathrm{pt}}$ into an equivalent surface magnetic

current density

$$\mathbf{M}_h^{\,\mathrm{pt}} \;=\; \frac{\nabla_h\times \mathbf{J}_z^{\,\mathrm{pt}}}{i\omega\epsilon} \;=\; \frac{i\omega\mu}{k^2}\,\delta(z-s)\frac{\partial}{\partial\rho}\left(\frac{\delta(\rho)}{\rho}\right)\hat{\mathbf{e}}_\rho, \tag{3.51}$$

where "$\nabla_h\times$" denotes the reduction of the curl operator to its $\partial(\cdot)/\partial\rho$ and $\partial(\cdot)/\partial\theta$ components. On recalling the fact that $\mathbf{M}_h^{\,\mathrm{pt}}$ can be described as a discontinuity in the tangential component of the $\mathbf{E}$ field across $z=s$, one finds by way of (3.12), (3.21), (3.40), (3.48) and (3.51) that the source terms in (3.24) and (3.43) due to $\mathbf{J}_h^{\,\mathrm{pt}}$ and $\mathbf{J}_z^{\,\mathrm{pt}}$ can be computed as

$$\begin{aligned}
&X_0^+ = -X_0^- = i\bar{\mu}_\ell, \quad X_m^+ = X_m^- = 0,\ m\neq 0,\\
&Y_{\pm1} = \pm i\bar{\mu}_\ell \bar{e}^{\mp i\theta_0}, \qquad U_{-1}^+ = -i\bar{\mu}_\ell\, e^{i\theta_0}, \quad U_1^- = i\bar{\mu}_\ell\, e^{-i\theta_0},\\
&Y_m = 0, m\neq\pm1, \qquad U_m^+ = 0, m\neq -1, \quad U_m^- = 0,\ m\neq 1.
\end{aligned} \tag{3.52}$$

3.4 Integral representation and evaluation

By way of the foregoing results, the spatial Green's functions in the j^{th} layer due to point-current excitation at $z=s,\ \rho=0$ can be shown to admit the integral

representation

$$E_\alpha^j = \frac{\omega\mu_\mathrm{o}k_\mathrm{o}}{2}\sum_{m=-1}^{1}\mathcal{J}_m\bigg[\int_0^\infty(\bar{u}_{1_m}^j+\bar{u}_{3_m}^j)\bar{\xi}J_{m+1}(\bar{\rho}\bar{\xi})\,\mathrm{d}\bar{\xi}$$
$$\pm\int_0^\infty(\bar{u}_{1_m}^j-\bar{u}_{3_m}^j)\bar{\xi}J_{m-1}(\bar{\rho}\bar{\xi})\,\mathrm{d}\bar{\xi}\bigg]e^{im\theta},$$
$$E_z^j = \omega\mu_\mathrm{o}k_\mathrm{o}\sum_{m=-1}^{1}\mathcal{J}_m\int_0^\infty\bar{u}_{2_m}^j\bar{\xi}J_m(\bar{\rho}\bar{\xi})\,\mathrm{d}\bar{\xi}\,e^{im\theta}, \tag{3.53}$$

in terms of the components of the $\mathbf{E}$ field, where $\alpha=\rho,\theta$; sign "+" (resp. "−") applies when $\alpha=\rho$ (resp. $\alpha=\theta$); $\mathcal{J}_{\pm1}=\mathcal{J}_h$; $\mathcal{J}_0=\mathcal{J}_z$, and $\mathcal{J}_h$ and $\mathcal{J}_z$ are the point-current source magnitudes defined in (3.48). On the basis of (3.11), (3.53) can be rewritten more compactly as

$$\mathbf{E}^j = \frac{\omega\mu_\mathrm{o}k_\mathrm{o}}{2}\sum_{\nu=0}^{2}\int_0^\infty\widetilde{\mathbf{E}^j}^\nu J_\nu(\bar{\rho}\bar{\xi})\,\mathrm{d}\bar{\xi}. \tag{3.54}$$

In a similar fashion, the $\mathbf{B}$ field can be computed as

$$\mathbf{B}^j = \frac{\mu_\mathrm{o}k_\mathrm{o}^2}{2}\sum_{\nu=0}^{2}\int_0^\infty\widetilde{\mathbf{B}^j}^\nu J_\nu(\bar{\rho}\bar{\xi})\,\mathrm{d}\bar{\xi}, \tag{3.55}$$

where the components of $\widetilde{\mathbf{B}^j}^\nu$ are related to $\bar{v}_{p_m}^j$ via (3.11).

3.4.1 Method of asymptotic decomposition

To evaluate (3.54) and (3.55) which are not amenable to closed-form integration, one may suitably decompose $\bar{v}_{p_m}^j$ and $\bar{v}_{p_m}^j$ as

$$\bar{u}_{p_m}^j = \bar{u}_{p_m}^{j,\mathrm{a}}+\bar{u}_{p_m}^{j,\mathrm{r}},\quad \bar{v}_{p_m}^j = \bar{v}_{p_m}^{j,\mathrm{a}}+\bar{v}_{p_m}^{j,\mathrm{r}},\quad p=1,2,3, \tag{3.56}$$

where $\bar{u}^{j,\mathrm{a}}_{p_m}$ and $\bar{v}^{j,\mathrm{a}}_{p_m}$ are respectively the *leading asymptotic behaviors* of $\bar{u}^{j}_{p_m}$ and $\bar{v}^{j}_{p_m}$ as $\bar{\xi} \to \infty$. The idea behind (3.56) is that the slow-decaying kernel components of (3.54) and (3.55) – namely $\bar{u}^{j,\mathrm{a}}_{p_m}$ and $\bar{v}^{j,\mathrm{a}}_{p_m}$, which are responsible for the singular behavior of $\mathbf{E}^j$ and $\mathbf{B}^j$ as the receiver approaches the source, be integrated analytically so that the remaining parts with strong integrand decay (in terms of $\bar{u}^{j,\mathrm{r}}_{p_m}$ and $\bar{v}^{j,\mathrm{r}}_{p_m}$) can be evaluated numerically. In what follows, a rigorous asymptotic analysis of the leading asymptotic terms demonstrates that $\bar{u}^{j,\mathrm{a}}_{p_m}$ and $\bar{v}^{j,\mathrm{a}}_{p_m}$ are, in physical terms, comprised of i) single and multiple "near-field" reflections that would occur in a suitably reduced layered system, and ii) direct "one-way" transmission from the source to receiver. Such reduction results in residual *field-form* Green's functions $\mathbf{E}^{j,\mathrm{r}}$ and $\mathbf{B}^{j,\mathrm{r}}$ whose kernels decay *as fast* as those of the *potential-form* counterparts, thus eliminating the perceived gap between the computation of the field forms and potential forms of the layered Green's functions in the spatial domain.

To expose the essence of (3.56), one may first employ (3.17), (3.18), (3.29) and (3.32) to express the solution within any layer in terms of the source-layer solution, (3.37) and (3.47). Such manipulation yields

$$\bar{u}^{j}_{1_m} = \frac{U^-_m - U^+_m}{4}\,\mathfrak{u}^{j}_{1,1},\ \ \bar{v}^{j}_{p_m} = \frac{U^+_m - U^-_m}{4}\,\mathfrak{v}^{j}_{p,1},\ \ p = 2, 3 \tag{3.57}$$

in terms of the TE-mode variables, where

$$\begin{aligned}
\mathfrak{u}^j_{1,1} &= \widehat{\mathcal{T}}^{\mathrm{E}}/\bar{\gamma}_\ell \cdot (\widehat{\mathcal{I}} + \widehat{\mathcal{R}}^{d,\mathrm{E}} + \widehat{\mathcal{R}}^{u,\mathrm{E}} + \widehat{\mathcal{R}}^{ud,\mathrm{E}}),\\
\mathfrak{v}^j_{2,1} &= \widehat{\mathcal{T}}^{\mathrm{E}}\bar{\xi}/\bar{\gamma}_\ell \cdot (\widehat{\mathcal{I}} + \widehat{\mathcal{R}}^{d,\mathrm{E}} + \widehat{\mathcal{R}}^{u,\mathrm{E}} + \widehat{\mathcal{R}}^{ud,\mathrm{E}}),\\
\mathfrak{v}^j_{3,1} &= \widehat{\mathcal{T}}^{\mathrm{E}}\bar{\gamma}_j/\bar{\gamma}_\ell \cdot (\pm\widehat{\mathcal{I}} - \widehat{\mathcal{R}}^{d,\mathrm{E}} + \widehat{\mathcal{R}}^{u,\mathrm{E}} \mp \widehat{\mathcal{R}}^{ud,\mathrm{E}}),
\end{aligned} \tag{3.58}$$

and

$$\begin{aligned}
\bar{v}^j_{1_m} &= \frac{X^+_m - X^-_m}{4}\,\mathfrak{v}^j_{1,0} + \frac{Y_m}{4}\,\mathfrak{v}^j_{1,1},\\
\bar{u}^j_{p_m} &= \frac{X^+_m - X^-_m}{4}\,\mathfrak{u}^j_{p,0} + \frac{Y_m}{4}\,\mathfrak{u}^j_{p,1},\ p = 2, 3,
\end{aligned} \tag{3.59}$$

in terms of the TM-mode variables where

$$\begin{aligned}
\mathfrak{v}^j_{1,0} &= \widehat{\mathcal{T}}^{\mathrm{M}}\bar{k}^2_j\bar{\xi}/(\bar{k}^2_\ell\bar{\gamma}_\ell) \cdot (\widehat{\mathcal{I}} + \widehat{\mathcal{R}}^{d,\mathrm{M}} + \widehat{\mathcal{R}}^{u,\mathrm{M}} + \widehat{\mathcal{R}}^{ud,\mathrm{M}}),\\
\mathfrak{v}^j_{1,1} &= \widehat{\mathcal{T}}^{\mathrm{M}}\bar{k}^2_j/\bar{k}^2_\ell \cdot (\pm\widehat{\mathcal{I}} + \widehat{\mathcal{R}}^{d,\mathrm{M}} - \widehat{\mathcal{R}}^{u,\mathrm{M}} \mp \widehat{\mathcal{R}}^{ud,\mathrm{M}}),\\
\mathfrak{u}^j_{2,0} &= \widehat{\mathcal{T}}^{\mathrm{M}}\bar{\xi}^2/(\bar{k}^2_\ell\bar{\gamma}_\ell) \cdot (\widehat{\mathcal{I}} + \widehat{\mathcal{R}}^{d,\mathrm{M}} + \widehat{\mathcal{R}}^{u,\mathrm{M}} + \widehat{\mathcal{R}}^{ud,\mathrm{M}}),\\
\mathfrak{u}^j_{2,1} &= \widehat{\mathcal{T}}^{\mathrm{M}}\bar{\xi}/\bar{k}^2_\ell \cdot (\pm\widehat{\mathcal{I}} + \widehat{\mathcal{R}}^{d,\mathrm{M}} - \widehat{\mathcal{R}}^{u,\mathrm{M}} \mp \widehat{\mathcal{R}}^{ud,\mathrm{M}}),\\
\mathfrak{u}^j_{3,0} &= \widehat{\mathcal{T}}^{\mathrm{M}}\bar{\xi}\bar{\gamma}_j/(\bar{k}^2_\ell\bar{\gamma}_\ell) \cdot (\pm\widehat{\mathcal{I}} - \widehat{\mathcal{R}}^{d,\mathrm{M}} + \widehat{\mathcal{R}}^{u,\mathrm{M}} \mp \widehat{\mathcal{R}}^{ud,\mathrm{M}}),\\
\mathfrak{u}^j_{3,1} &= \widehat{\mathcal{T}}^{\mathrm{M}}\bar{\gamma}_j/\bar{k}^2_\ell \cdot (\widehat{\mathcal{I}} - \widehat{\mathcal{R}}^{d,\mathrm{M}} - \widehat{\mathcal{R}}^{u,\mathrm{M}} + \widehat{\mathcal{R}}^{ud,\mathrm{M}}).
\end{aligned} \tag{3.60}$$

On omitting the tags "E" and "M" for brevity, (3.58) and (3.60) are completed by

specifying that sign "+" and

$$\begin{aligned}
\widehat{\mathcal{T}} &= \left(1-\widehat{R}^u_{\ell-1}\widehat{R}^d_\ell\mathcal{E}_\ell^2\right)^{-1}\widehat{T}^d_{j-1}\cdots\widehat{T}^d_\ell,\\
\widehat{\mathcal{I}} &= (\mathcal{E}_{j-1}\cdots\mathcal{E}_\ell)e^{-\bar{\gamma}_\ell(\bar{z}_{\ell-1}-\bar{s})-\bar{\gamma}_j(\bar{z}-\bar{z}_{j-1})},\\
\widehat{\mathcal{R}}^d &= \widehat{R}^d_j(\mathcal{E}_{j-1}\cdots\mathcal{E}_\ell)e^{-\bar{\gamma}_\ell(\bar{z}_{\ell-1}-\bar{s})-\bar{\gamma}_j(2\bar{z}_j+\bar{z}-\bar{z}_{j-1})},\\
\widehat{\mathcal{R}}^u &= \widehat{R}^u_{\ell-1}(\mathcal{E}_{j-1}\cdots\mathcal{E}_\ell)e^{-\bar{\gamma}_\ell(\bar{s}-\bar{z}_{\ell-1})-\bar{\gamma}_j(\bar{z}-\bar{z}_{j-1})},\\
\widehat{\mathcal{R}}^{ud} &= \widehat{R}^d_j\widehat{R}^u_{\ell-1}(\mathcal{E}_{j-1}\cdots\mathcal{E}_\ell)e^{-\bar{\gamma}_\ell(\bar{s}-\bar{z}_{\ell-1})-\bar{\gamma}_j(2\bar{z}_j+\bar{z}-\bar{z}_{j-1})},
\end{aligned} \tag{3.61}$$

are taken when $\bar{z}\geqslant\bar{s}$, whereas sign "−" and

$$\begin{aligned}
\widehat{\mathcal{T}} &= \left(1-\widehat{R}^u_{\ell-1}\widehat{R}^d_\ell\mathcal{E}_\ell^2\right)^{-1}\widehat{T}^u_j\cdots\widehat{T}^u_{\ell-1},\\
\widehat{\mathcal{I}} &= (\mathcal{E}_{j+1}\cdots\mathcal{E}_\ell)e^{-\bar{\gamma}_\ell(\bar{s}-\bar{z}_\ell)-\bar{\gamma}_j(\bar{z}_j-\bar{z})},\\
\widehat{\mathcal{R}}^d &= \widehat{R}^d_\ell(\mathcal{E}_{j+1}\cdots\mathcal{E}_\ell)e^{-\bar{\gamma}_\ell(\bar{z}_\ell-\bar{s})-\bar{\gamma}_j(\bar{z}_j-\bar{z})},\\
\widehat{\mathcal{R}}^u &= \widehat{R}^u_{j-1}(\mathcal{E}_{j+1}\cdots\mathcal{E}_\ell)e^{-\bar{\gamma}_\ell(\bar{s}-\bar{z}_\ell)-\bar{\gamma}_j(\bar{z}_j+\bar{z}-2\bar{z}_{j-1})},\\
\widehat{\mathcal{R}}^{ud} &= \widehat{R}^d_\ell\widehat{R}^u_{j-1}(\mathcal{E}_{j+1}\cdots\mathcal{E}_\ell)e^{-\bar{\gamma}_\ell(\bar{z}_\ell-\bar{s})-\bar{\gamma}_j(\bar{z}_j+\bar{z}-2\bar{z}_{j-1})},
\end{aligned} \tag{3.62}$$

apply when $\bar{z}<\bar{s}$.

With (3.57)–(3.62) in place, the evaluation of $\bar{u}^{j,\mathrm{a}}_{p_m}$ and $\bar{v}^{j,\mathrm{a}}_{p_m}$ can be carried out in a number of ways, depending on how much similarity is required between the overall response and its asymptotic expansion. With reference to (3.56), the three *key requirements* are that: i) the residual integrals featuring $\bar{u}^{j,\mathrm{r}}_{p_m}$ and $\bar{v}^{j,\mathrm{r}}_{p_m}$ remain *regular* as the observation point approaches the source; ii) $\bar{u}^{j,\mathrm{r}}_{p_m}$ and $\bar{v}^{j,\mathrm{r}}_{p_m}$

exhibit *rapid decay* (beyond what is needed to meet the first requirement) for the purposes of effective numerical integration, and iii) that the singular components of $\mathbf{E}^j$ and $\mathbf{B}^j$, featuring $\bar{u}_{p_m}^{j,\mathrm{a}}$ and $\bar{v}_{p_m}^{j,\mathrm{a}}$, are integrable in *closed-form*. To meet such demands, the approach adopted here is based on the treatment of potential-form Green's functions in [22], where the singular "near-field" effects within given layered structure are approximated by those generated in a suitably constructed *three-layer* system, composed of a single stratum with two adjacent half-spaces. In this way, when the source and receiver are in the same layer ($j = \ell$), $\bar{u}_{p_m}^{\ell,\mathrm{a}}$ and $\bar{v}_{p_m}^{\ell,\mathrm{a}}$ are computed by taking into account the direct arrival and suitable number of reflections from the upper ($\bar{z}_{\mathrm{upp}-1} = \bar{z}_{\ell-1}$) and lower ($\bar{z}_{\mathrm{low}} = \bar{z}_{\ell}$) interfaces as shown in Fig. 3.3(b). When the source and receiver are in different layers ($j \neq \ell$), on the other hand, $\bar{u}_{p_m}^{j,\mathrm{a}}$ and $\bar{v}_{p_m}^{j,\mathrm{a}}$ can be extracted in a similar fashion by: 1) specifying $\bar{z}_{\mathrm{upp}-1} = \bar{z}_{\min\{\ell-1,j-1\}}$ and $\bar{z}_{\mathrm{low}} = \bar{z}_{\max\{\ell,j\}}$, and 2) computing the direct arrival via a product of relevant transmission coefficients between layers ℓ and j, see Fig. 3.3(a).

To compute the sought asymptotic expansions on the basis of the foregoing three-layer scheme, one may first note that

$$\mathcal{E}_\ell = e^{-\bar{\gamma}_\ell \bar{h}_\ell} = O(e^{-\bar{\xi}\bar{h}_\ell}) \quad \text{as} \quad \bar{\xi} \to \infty, \tag{3.63}$$

which permits the generalized transmission and reflection coefficients (see (3.30)

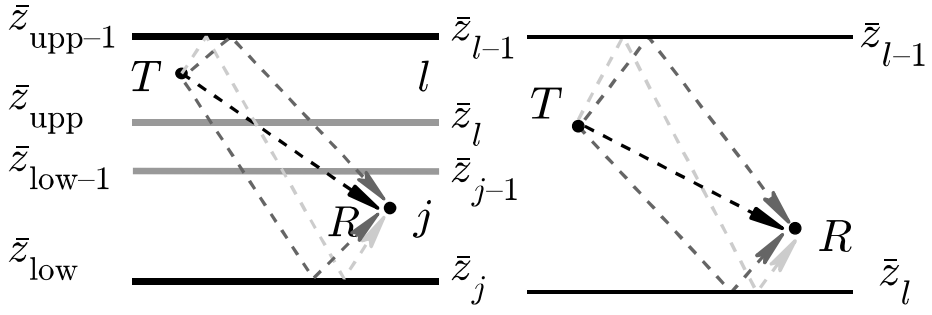

(a) $j \neq l$ (b) $j = l$

Figure 3.3: Physical description of the three-layer asymptotic extraction.

and (3.33)) to be approximated by constants

$$\lim_{\bar{\xi}\to\infty} \widehat{R}_j^{\star,\diamond} = \mathsf{R}_j^{\star,\diamond}, \qquad \lim_{\bar{\xi}\to\infty} \widehat{T}_j^{\star,\diamond} = \mathsf{T}_j^{\star,\diamond}, \tag{3.64}$$

where $\star = u, d,\ \diamond = \text{E}, \text{M}$. In (3.64), the explicit expressions for $\mathsf{R}_j^{\star,\diamond}$ and $\mathsf{T}_j^{\star,\diamond}$ can be shown as

$$\mathsf{R}_j^{u,\text{E}} = \frac{\bar{\mu}_j - \bar{\mu}_{j+1}}{\bar{\mu}_j + \bar{\mu}_{j+1}}, \mathsf{R}_j^{d,\text{E}} = \frac{\bar{\mu}_{j+1} - \bar{\mu}_j}{\bar{\mu}_j + \bar{\mu}_{j+1}}, \mathsf{R}_j^{u,\text{M}} = \frac{\bar{\epsilon}_j - \bar{\epsilon}_{j+1}}{\bar{\epsilon}_j + \bar{\epsilon}_{j+1}}, \mathsf{R}_j^{d,\text{M}} = \frac{\bar{\epsilon}_{j+1} - \bar{\epsilon}_j}{\bar{\epsilon}_j + \bar{\epsilon}_{j+1}},$$
$$\mathsf{T}_j^{u,\text{E}} = \frac{2\bar{\mu}_j}{\bar{\mu}_j + \bar{\mu}_{j+1}}, \mathsf{T}_j^{d,\text{E}} = \frac{2\bar{\mu}_{j+1}}{\bar{\mu}_j + \bar{\mu}_{j+1}}, \mathsf{T}_j^{u,\text{M}} = \frac{2\bar{\epsilon}_{j+1}}{\bar{\epsilon}_j + \bar{\epsilon}_{j+1}}, \mathsf{T}_j^{d,\text{M}} = \frac{2\bar{\epsilon}_j}{\bar{\epsilon}_j + \bar{\epsilon}_{j+1}}.$$

Expansion coefficients in formulas (3.68):

$$C_1 = \mathsf{R}^d_\ell, \qquad C_2 = \tfrac{1}{2}\bar{d}_2\bar{k}^2_\ell\mathsf{R}^d_\ell, \qquad C_3 = \big(\tfrac{1}{8}\bar{d}^2_2\bar{k}^4_\ell + \tfrac{1}{2}\bar{k}^2_\ell\big)\mathsf{R}^d_\ell + \mathfrak{C}_{\ell+1},$$

$$C_4 = \mathsf{R}^u_{\ell-1}, \qquad C_5 = \tfrac{1}{2}\bar{d}_3\bar{k}^2_1\mathsf{R}^u_{\ell-1}, \qquad C_6 = \big(\tfrac{1}{8}\bar{d}^2_3\bar{k}^4_\ell + \tfrac{1}{2}\bar{k}^2_\ell\big)\mathsf{R}^u_{\ell-1} + \mathfrak{C}_{\ell-1},$$

$$C_7 = \mathsf{R}^d_\ell\mathsf{R}^u_{\ell-1}, \qquad C_8 = \tfrac{1}{2}\bar{d}_4\bar{k}^2_1\mathsf{R}^d_\ell\mathsf{R}^u_{\ell-1},$$

$$C_9 = \big(\tfrac{1}{8}\bar{d}^2_4\bar{k}^4_\ell + \tfrac{1}{2}\bar{k}^2_\ell\big)\mathsf{R}^d_\ell\mathsf{R}^u_{\ell-1} + \mathfrak{C}_{\ell+1}\mathsf{R}^u_{\ell-1} + \mathfrak{C}_{\ell-1}\mathsf{R}^d_\ell,$$

$$C_{10} = \tfrac{1}{8}\bar{d}^2_2\bar{k}^4_\ell\mathsf{R}^d_\ell + \mathfrak{C}_{\ell+1}, \qquad C_{11} = \tfrac{1}{8}\bar{d}^2_3\bar{k}^4_\ell\mathsf{R}^u_{\ell-1} + \mathfrak{C}_{\ell-1},$$

$$C_{12} = \tfrac{1}{8}\bar{d}^2_4\bar{k}^4_\ell\mathsf{R}^d_\ell\mathsf{R}^u_{\ell-1} + \mathfrak{C}_{\ell+1}\mathsf{R}^u_{\ell-1} + \mathfrak{C}_{\ell-1}\mathsf{R}^d_\ell,$$

$$C_{13} = \big(\tfrac{1}{8}\bar{d}^2_2\bar{k}^4_\ell - \tfrac{1}{2}\bar{k}^2_\ell\big)\mathsf{R}^d_\ell + \mathfrak{C}_{\ell+1}, \qquad C_{14} = \big(\tfrac{1}{8}\bar{d}^2_3\bar{k}^4_\ell - \tfrac{1}{2}\bar{k}^2_\ell\big)\mathsf{R}^u_{\ell-1} + \mathfrak{C}_{\ell-1},$$

$$C_{15} = \big(\tfrac{1}{8}\bar{d}^2_4\bar{k}^4_\ell - \tfrac{1}{2}\bar{k}^2_\ell\big)\mathsf{R}^d_\ell\mathsf{R}_{\ell-1} + \mathfrak{C}_{\ell+1}\mathsf{R}^u_{\ell-1} + \mathfrak{C}_{\ell-1}\mathsf{R}^d_\ell,$$

where

$$\mathfrak{C}_{\ell+1} = \frac{p_\ell p_{\ell+1}(\bar{k}^2_{\ell+1} - \bar{k}^2_\ell)}{(p_\ell + p_{\ell+1})^2}, \;\; \mathfrak{C}_{\ell-1} = \frac{p_\ell p_{\ell-1}(\bar{k}^2_{\ell-1} - \bar{k}^2_\ell)}{(p_\ell + p_{\ell-1})^2},$$

noting that $p = \bar{\epsilon}$ for the TM mode and $p = \bar{\mu}$ for the TE mode.

Case $j \neq l$

On dropping the "E" and "M" tags for brevity and assuming the receiver and the source to be in different layers (see Fig. 3.3(a)), the leading asymptotic behavior of (3.61) and (3.62) can be shown to permit the representation

$$\begin{gathered}\widehat{\mathcal{T}}^{\mathrm{a}} = \prod_{m=\ell}^{j-1}\mathsf{T}^d_m, \quad \widehat{\mathcal{I}}^{\mathrm{a}} = \mathfrak{e}_1, \\ \widehat{\mathcal{R}}^{d,\mathrm{a}} = \mathsf{R}^d_j\mathfrak{e}_2, \;\; \widehat{\mathcal{R}}^{u,\mathrm{a}} = \mathsf{R}^u_{\ell-1}\mathfrak{e}_3, \;\; \widehat{\mathcal{R}}^{ud,\mathrm{a}} = \mathsf{R}^d_j\mathsf{R}^u_{\ell-1}\mathfrak{e}_4,\end{gathered} \tag{3.65}$$

when $\bar{z} \geq \bar{s}$, and

$$\begin{gathered} \widehat{\mathcal{T}}^{\mathrm{a}} = \prod_{m=j}^{\ell-1} \mathsf{T}_m^u, \quad \widehat{\mathcal{I}}^{\mathrm{a}} = \mathfrak{e}_1, \\ \widehat{\mathcal{R}}^{d,\mathrm{a}} = \mathsf{R}_\ell^d \mathfrak{e}_2, \quad \widehat{\mathcal{R}}^{u,\mathrm{a}} = \mathsf{R}_{j-1}^u \mathfrak{e}_3, \quad \widehat{\mathcal{R}}^{ud,\mathrm{a}} = \mathsf{R}_\ell^d \mathsf{R}_{j-1}^u \mathfrak{e}_4, \end{gathered} \tag{3.66}$$

when $\bar{z} < \bar{s}$. Here

$$\mathfrak{e}_i = e^{-\bar{\xi}\bar{d}_i}, \quad \bar{d}_1 = |\bar{z} - \bar{s}|, \quad \bar{d}_2 = 2\bar{z}_{\mathrm{low}} - (\bar{s} + \bar{z}),$$

$$\bar{d}_3 = \bar{s} + \bar{z} - \bar{z}_{\mathrm{upp}-1}, \qquad \bar{d}_4 = 2(\bar{z}_{\mathrm{low}} - \bar{z}_{\mathrm{upp}-1}) - \bar{d}_1,$$

while $\bar{z}_{\mathrm{upp}-1} = \bar{z}_{\min\{\ell-1, j-1\}}$ and $\bar{z}_{\mathrm{low}} = \bar{z}_{\max\{\ell, j\}}$ as examined earlier.

With (3.56)–(3.62), (3.65) and (3.66) at hand, the asymptotic components of (3.54) and (3.55) can be computed in *closed-form* by evaluating the canonical integrals

$$\mathrm{CI}_\nu^n = \int_0^\infty \bar{\xi}^n e^{-\bar{\xi}\bar{z}} J_\nu(\bar{\rho}\bar{\xi})\, \mathrm{d}\bar{\xi}, \qquad n + \nu > -1, \tag{3.67}$$

noting in particular that CI_ν^0, CI_ν^1 and CI_ν^2 can be obtained by way of the integral identities in [24].

Case $j = l$

When the source and receiver are in the same layer as shown in Fig. 3.3(b), the leading asymptotic behavior of (3.61) and (3.62) can be computed via expansions

$\widehat{\mathcal{T}}^{\mathrm{a}} = 1,\ \widehat{\mathcal{I}}^{\mathrm{a}} = \mathfrak{e}_1$, and

$$\begin{aligned}
&\left[\tfrac{\bar{\xi}}{\bar{\gamma}_\ell}\widehat{\mathcal{R}}^d\right]^{\mathrm{a}} = C_{1,2,3}\mathfrak{e}_2,\ \left[\widehat{\mathcal{R}}^d\right]^{\mathrm{a}} = C_{1,2,10}\mathfrak{e}_2,\ \left[\tfrac{\bar{\gamma}_\ell}{\bar{\xi}}\widehat{\mathcal{R}}^d\right]^{\mathrm{a}} = C_{1,2,13}\mathfrak{e}_2,\\
&\left[\tfrac{\bar{\xi}}{\bar{\gamma}_\ell}\widehat{\mathcal{R}}^u\right]^{\mathrm{a}} = C_{4,5,6}\mathfrak{e}_3,\ \left[\widehat{\mathcal{R}}^u\right]^{\mathrm{a}} = C_{4,5,11}\mathfrak{e}_3,\ \left[\tfrac{\bar{\gamma}_\ell}{\bar{\xi}}\widehat{\mathcal{R}}^u\right]^{\mathrm{a}} = C_{4,5,14}\mathfrak{e}_3,\\
&\left[\tfrac{\bar{\xi}}{\bar{\gamma}_\ell}\widehat{\mathcal{R}}^{ud}\right]^{\mathrm{a}} = C_{7,8,9}\mathfrak{e}_4,\left[\widehat{\mathcal{R}}^{ud}\right]^{\mathrm{a}} = C_{7,8,12}\mathfrak{e}_4,\left[\tfrac{\bar{\gamma}_\ell}{\bar{\xi}}\widehat{\mathcal{R}}^{ud}\right]^{\mathrm{a}} = C_{7,8,15}\mathfrak{e}_4,
\end{aligned} \tag{3.68}$$

where $C_{i,j,k} = C_i + C_j\bar{\xi}^{-1} + C_k\bar{\xi}^{-2}$, with the expressions for $C_i (i = 1, \cdots, 15)$ given in Appendix. In this case, however, integrals of form (3.67) are insufficient to capture the singularity of the Green's functions associated with the direct arrival. To repel the problem, all integrals containing the direct-arrival term $\widehat{\mathcal{I}} = e^{-\bar{\gamma}_\ell \bar{d}_1}$ are computed (without approximation) in closed form via their decomposition in Sommerfeld integrals (SI), namely

$$\mathrm{SI}_\nu^{n,m} = \int_0^\infty \bar{\xi}^n \bar{\gamma}^m e^{-\bar{\gamma}\bar{z}} J_\nu(\bar{\rho}\bar{\xi})\,\mathrm{d}\bar{\xi}, \qquad \nu = 0, 1, 2 \tag{3.69}$$

where the necessary SI's are $\mathrm{SI}_0^{1,1}$, $\mathrm{SI}_2^{1,1}$, $\mathrm{SI}_0^{1,-1}$, $\mathrm{SI}_2^{1,-1}$, $\mathrm{SI}_0^{3,-1}$, $\mathrm{SI}_1^{2,-1}$, $\mathrm{SI}_0^{1,0}$, $\mathrm{SI}_2^{1,0}$, and $\mathrm{SI}_1^{2,0}$ whose closed-form expressions are available in [25]. The remaining terms, containing the expanded reflection coefficients, are evaluated via (3.67) as before.

3.4.2 Numerical scheme to evaluate the residual component

On the basis of (3.56) and the featured three-layer asymptotic extraction, $\bar{u}_{p_m}^{j,\mathrm{r}}$ and $\bar{v}_{p_m}^{j,\mathrm{r}}$ exhibit rapid decay as $\bar{\xi} \to \infty$ regardless of the source-receiver distance.

In particular, it follows from the results in Sec. 3.4.1 that $\bar{u}_{p_m}^{j,\mathrm{r}}$ and $\bar{v}_{p_m}^{j,\mathrm{r}}$ behave as $O(\bar{\xi}^{-\alpha}),\ \alpha > 2$, as $\bar{\xi} \to \infty$ which is commensurate with the decay of the respective *potential-form* residual kernels in [22]. From (3.53) and its magnetic field counterpart, it thus follows that the improper integrals comprising the residual components of (3.54) and (3.55) remain *unconditionally regular* and can be consistently approximated as

$$f = \int_0^{\infty} \widetilde{f}(\bar{\xi}) J_\nu(\bar{\rho}\bar{\xi}) d\bar{\xi} \ \approx \ \int_0^{\bar{\xi}_{\max}} \widetilde{f}(\bar{\xi}) J_\nu(\bar{\rho}\bar{\xi}) d\bar{\xi}, \tag{3.70}$$

for all source-receiver pairs, where $\widetilde{f}(\bar{\xi})$ are expressible in terms of $\bar{u}_{p_m}^{j,\mathrm{r}}$ and $\bar{v}_{p_m}^{j,\mathrm{r}}$ while $\bar{\xi}_{\max}$ is the unique point of truncation, commensurate with the sought approximation accuracy. In devising a numerical scheme to evaluate the "pruned" integrals in (3.70), one should however keep in mind that ($\bar{u}_{p_m}^{j}$ and $\bar{v}_{p_m}^{j}$ and thus) $\bar{u}_{p_m}^{j,\mathrm{r}}$ and $\bar{v}_{p_m}^{j,\mathrm{r}}$ generally have a number of *poles* in the complex $\bar{\xi}$-plane (including the positive real axis) whose locations are given by the roots of the characteristic equation

$$1 - \widehat{R}_{n-1}^{u,\diamond} \widehat{R}_n^{d,\diamond} \mathcal{E}_n^2 \ = \ 0, \qquad \diamond = \mathrm{E}, \mathrm{M}, \tag{3.71}$$

see also [26] in the context of horizontally-polarized seismic waves. Physically, the positive real roots of (3.71) are the wavenumbers corresponding to guided-wave modes in a given layered structure at prescribed frequency of excitation [11]. On taking the reference wave number k_{o} as that corresponding to the free space with

properties of the "slowest" layer *i.e.* $k_{\rm o}=\omega\max_j\{{\rm Re}(\sqrt{\mu_j\epsilon_j})\}$, it can be shown as in [27] that the real roots of (3.71), in terms of $\bar{\xi}=\xi/k_{\rm o}$, are bounded *from above* by unity. By making reference to the analyticity of the residual integrands in (3.70) and the choice of branch cuts for $\bar{\gamma}_j$ as in Fig. 3.1, the path of numerical integration can accordingly be deformed into part of the fourth quadrant, see Fig. 3.4, to avoid the featured surface-wave singularities. In light of the aforestated upper bound on the real-valued roots of (3.71), such contour can be conveniently set so that it safely reunites with the Re($\bar{\xi}$)-axis at $\bar{\xi}_c$, say $\bar{\xi}_c=1.2$.

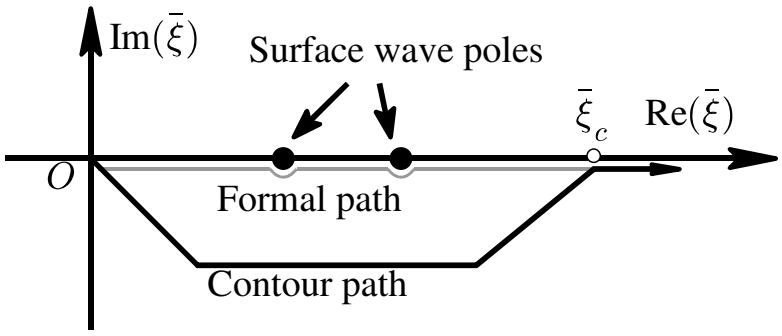

Figure 3.4: Modified contour path of integration.

Following the treatment of horizontally-polarized seismic waves in [26], the truncated contour path of integration is, for numerical purposes, subdivided into a number of intervals. Over each (straight-line) interval, integrands $\widetilde{f}(\bar{\xi})$ in (3.70) are approximated via eight-point Lagrange interpolation [28] as

$$\widetilde{f}(\bar{\xi}) \;=\; \mathbf{F}^{\rm T}\mathbf{C}\,\mathbf{Z}(\bar{\xi}),$$

where $\mathbf{C}$ is an 8×8 coefficient matrix;

$$\mathbf{F}^{\mathrm{T}} = \big[\widetilde{f}(\bar{\xi}_{-3}), \widetilde{f}(\bar{\xi}_{-2}), \cdots, \widetilde{f}(\bar{\xi}_{4})\big],$$
$$\mathbf{Z}^{\mathrm{T}} = \left[1, \Big(\frac{\bar{\xi}-\bar{\xi}_0}{\Delta}\Big), \cdots, \Big(\frac{\bar{\xi}-\bar{\xi}_0}{\Delta}\Big)^7\right],\ \Delta = \tfrac{1}{7}(\bar{\xi}_4 - \bar{\xi}_{-3}),$$

and $\bar{\xi}_k$ ($k = -3, \ldots 4$) are equidistant collocation points. With the aid of the series representation of Bessel functions [28] for small-to-moderate arguments, namely

$$J_\nu(x) = \Big(\frac{x}{2}\Big)^\nu \sum_{i=0}^{\infty} \frac{(-x^2/4)^i}{i!(\nu+i)!},$$

integral $\int_{\bar{\xi}_{-3}}^{\bar{\xi}_4} \mathbf{Z} J_\nu(\bar{\rho}\bar{\xi})\,\mathrm{d}\bar{\xi}$ can be evaluated analytically as

$$\int_{\bar{\xi}_{-3}}^{\bar{\xi}_4} \Big(\frac{\bar{\xi}-\bar{\xi}_0}{\Delta}\Big)^k J_\nu(\bar{\rho}\bar{\xi})\,\mathrm{d}\bar{\xi} = \sum_{n=0}^{k} \binom{k}{n} \frac{(-\bar{\xi}_0)^n}{\Delta^k} \times \sum_{i=0}^{\infty} \Big(\frac{\bar{\rho}\,\bar{\xi}}{2}\Big)^{2i+\nu} \frac{(-1)^i}{i!(i+\nu)!}\, \frac{\bar{\xi}^{k-n+1}}{2i+\nu+k-n+1}\Bigg|_{\bar{\xi}_{-3}}^{\bar{\xi}_4}.$$

For large arguments of the Bessel function, on the other hand, one has

$$J_\nu(x) \approx \sqrt{\frac{2}{\pi x}} \Big\{ [P(\nu,x)\cos\phi + Q(\nu,x)\sin\phi]\cos x + [P(\nu,x)\sin\phi - Q(\nu,x)\cos\phi]\sin x \Big\},$$

where $\varphi = (\frac{\nu}{2} + \frac{1}{4})\pi$ [28], so that

$$\widetilde{f}(\bar{\xi}) J_\nu(\bar{\rho}\bar{\xi}) \;=\; \mathbf{F}^{\mathrm{T}}\mathbf{P}\,\mathbf{C}\,\mathbf{Z}(\bar{\xi})\cos(\bar{\rho}\bar{\xi}) + \mathbf{F}^{\mathrm{T}}\mathbf{Q}\,\mathbf{C}\,\mathbf{Z}(\bar{\xi})\sin(\bar{\rho}\bar{\xi}),$$

with

$$\mathbf{P} = \mathrm{diag}\Big[\sqrt{2/(\pi\bar{\rho}\bar{\xi}_k)}\big(P(\nu,\bar{\rho}\bar{\xi}_k)\cos\varphi + Q(\nu,\bar{\rho}\bar{\xi}_k)\sin\varphi\big)\Big],$$
$$\mathbf{Q} = \mathrm{diag}\Big[\sqrt{2/(\pi\bar{\rho}\bar{\xi}_k)}\big(P(\nu,\bar{\rho}\bar{\xi}_k)\sin\varphi - Q(\nu,\bar{\rho}\bar{\xi}_k)\cos\varphi\big)\Big].$$

Here integrals $\int_{\bar{\xi}_{-3}}^{\bar{\xi}_4} \mathbf{Z}\cos(\bar{\rho}\bar{\xi})\,\mathrm{d}\bar{\xi}$ and $\int_{\bar{\xi}_{-3}}^{\bar{\xi}_4} \mathbf{Z}\sin(\bar{\rho}\bar{\xi})\,\mathrm{d}\bar{\xi}$ can be computed as

$$\int_{\bar{\xi}_{-3}}^{\bar{\xi}_4} \Big(\frac{\bar{\xi}-\bar{\xi}_0}{\Delta}\Big)^k \begin{Bmatrix} \cos(\bar{\rho}\bar{\xi}) \\ \\ \sin(\bar{\rho}\bar{\xi}) \end{Bmatrix} \mathrm{d}\bar{\xi} = \pm \sum_{n=0}^{k} \binom{k}{n} \frac{(-\bar{\xi}_0)^n}{\Delta^k}$$

$$\times \sum_{i=0}^{k-n} i! \binom{k-n}{i} \frac{\bar{\xi}^{k-n-i}}{\bar{\rho}^{i+1}} \begin{Bmatrix} \sin(\bar{\rho}\bar{\xi}+i\pi/2) \\ \\ \cos(\bar{\rho}\bar{\xi}+i\pi/2) \end{Bmatrix} \Bigg|_{\bar{\xi}_{-3}}^{\bar{\xi}_4}.$$

As a result, (3.70) can be integrated analytically over the truncated contour path as

$$\begin{aligned} f \approx & \sum_{\substack{\text{intvls.with} \\ \text{small } \bar{\xi}}} \mathbf{F}^{\mathrm{T}}\mathbf{C} \int_{\bar{\xi}_{-3}}^{\bar{\xi}_4} \mathbf{Z}(\bar{\xi}) J_\nu(\bar{\rho}\bar{\xi})\,\mathrm{d}\bar{\xi} \\ & + \sum_{\substack{\text{intvls.with} \\ \text{large } \bar{\xi}}} \left[\mathbf{F}^{\mathrm{T}}\mathbf{P}\mathbf{C} \int_{\bar{\xi}_{-3}}^{\bar{\xi}_4} \mathbf{Z}(\bar{\xi})\cos(\bar{\rho}\bar{\xi})\,\mathrm{d}\bar{\xi} + \mathbf{F}^{\mathrm{T}}\mathbf{Q}\mathbf{C} \int_{\bar{\xi}_{-3}}^{\bar{\xi}_4} \mathbf{Z}(\bar{\xi})\sin(\bar{\rho}\bar{\xi})\,\mathrm{d}\bar{\xi} \right]. \end{aligned} \quad (3.72)$$

To deal with the complexity of residual functions $\bar{u}_{p_m}^{j,\mathrm{r}}$ and $\bar{v}_{p_m}^{j,\mathrm{r}}$ in a robust fashion for an arbitrary layered structure, (3.72) is applied in a *recursive fashion* that repeatedly halves the interval size, Δ, until the target accuracy is achieved. Here it is noted that: i) the featured integration of Bessel functions notably reduces the sensitivity of the numerical scheme to the radial distance, and ii) the numerical interpolation approach, while nominally less efficient than the corresponding Gaussian quadrature, carries significant advantage in terms of the proposed adaptive integration scheme. In particular when halving Δ, the Gaussian scheme cannot take advantage of the existing N evaluations and requires $2N$ new evaluations of

the kernel. In contrast, the featured interpolation scheme requires only N new evaluations to achieve the commensurate effect.

3.5 Results

In what follows, the effectiveness of the proposed analytical and computational treatment is verified via comparisons with available results. In the first example, simulations are performed to compute the electric and magnetic response of a two-half-space structure (air: $\mathcal{L}_0$ and sea: $\mathcal{L}_1$) due to vertical and horizontal electric dipole (VED and HED) radiation at 600 MHz. The results are compared to those in [25], who obtained the analytical solution to the problem under certain simplifying hypotheses which require that $k_1\rho \geqslant 3$. To examine the efficacy of the asymptotic decomposition scheme, it is assumed that both the source and the receiver are located *at the air-sea interface* (by taking the limit from either the top or the bottom half-space), in which case the integrands in (3.54) and (3.55) are clear of exponential decay under both VED and HED radiation. With reference to (3.2), the air region is characterized by parameters ε_0, μ_0 and $\sigma_0 = 0$, while the sea region is characterized by $\varepsilon_1 = 80\varepsilon_0$, $\mu_1 = \mu_0$ and $\sigma_1 = 3.5\,\mathrm{S/m}$ (note that the normalization constants are taken as $\epsilon_{\mathrm{o}} = [\mathrm{Re}(\sqrt{\varepsilon_1 + i\sigma_1/\omega})]^2$ and $\mu_{\mathrm{o}} = \mu_1$ following earlier discussion). The radial separation, ρ, between the source and

receiver varies from 1 cm to 100 m.

For VED radiation, the source is located on the air side of the interface, and the corresponding results are denoted by subscript "0V". Due to axial symmetry of the problem, only the radial and vertical components of the electric field exist as shown in Fig. 3.5. For HED radiation, on the other hand, the source is located on the sea side of the interface (acting in the $\theta_0 = 0$ direction), and the associated results are denoted by index "1H'. In Fig. 3.6, the results are plotted for all three components of the electric filed when the receiver is on either side of the interface.

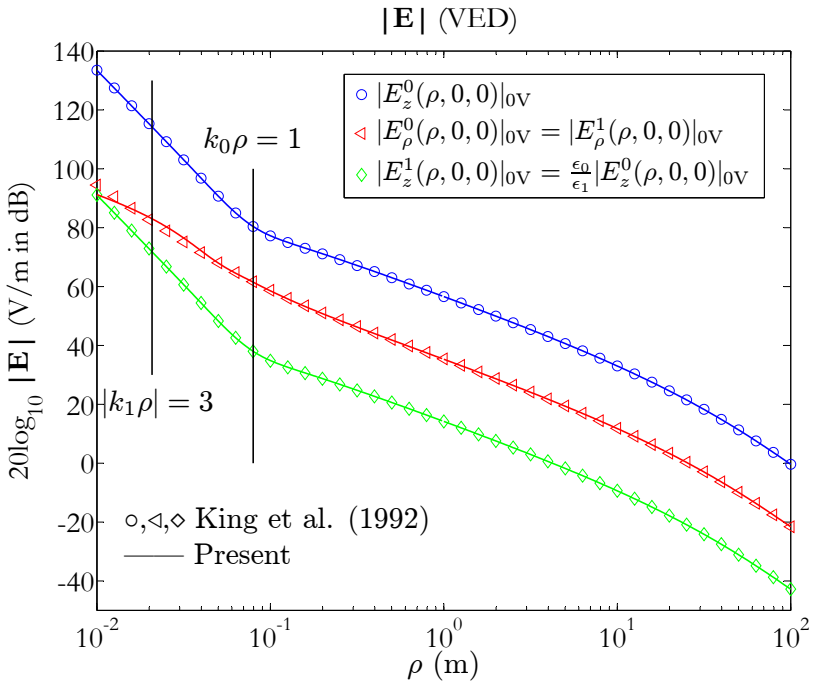

Figure 3.5: Electric field due to VED acting on the air side of the interface.

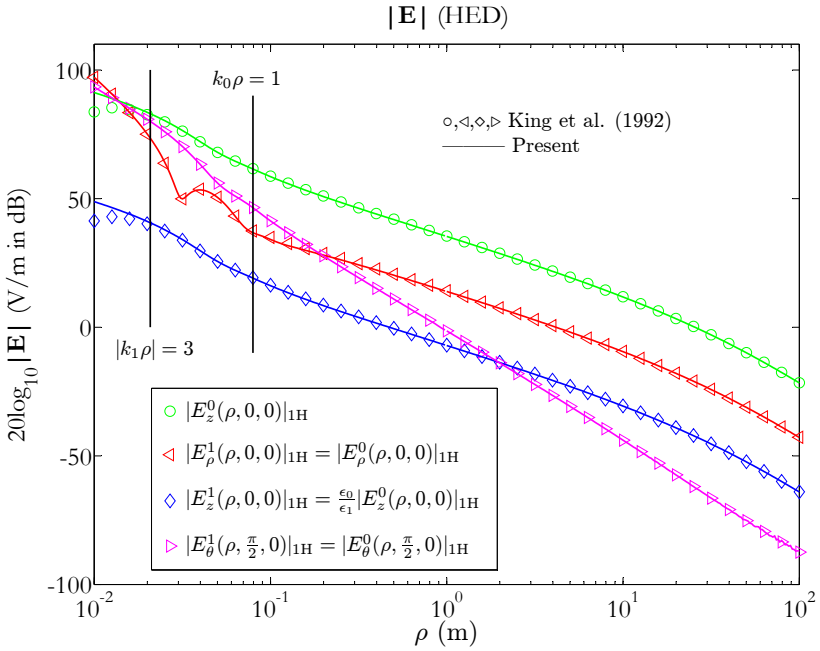

Figure 3.6: Electric field due to HED acting on the sea side of the interface.

For completeness, Fig. 3.7 compares the respective magnetic field responses, noting that only the azimuthal component exists in the VED case, whereas all three components enter the HED calculations. As shown in the display, the magnitude of the magnetic field response is plotted on the air (resp. sea) side of the interface for the problem of VED (resp. HED) radiation.

As can be seen from Figs. 3.5–3.7, there is a good agreement between the present results and those in [25] (in terms of all relevant components of $\mathbf{E}^j$ and $\mathbf{B}^j$, $j = 1, 2$) all the way down to the aforementioned threshold, $k_1\rho = 3$, below which the analytical solution ceases to apply. For completeness, all three panels also include an auxiliary threshold $k_0\rho = 1$ that, following [25], signifies a demarcation

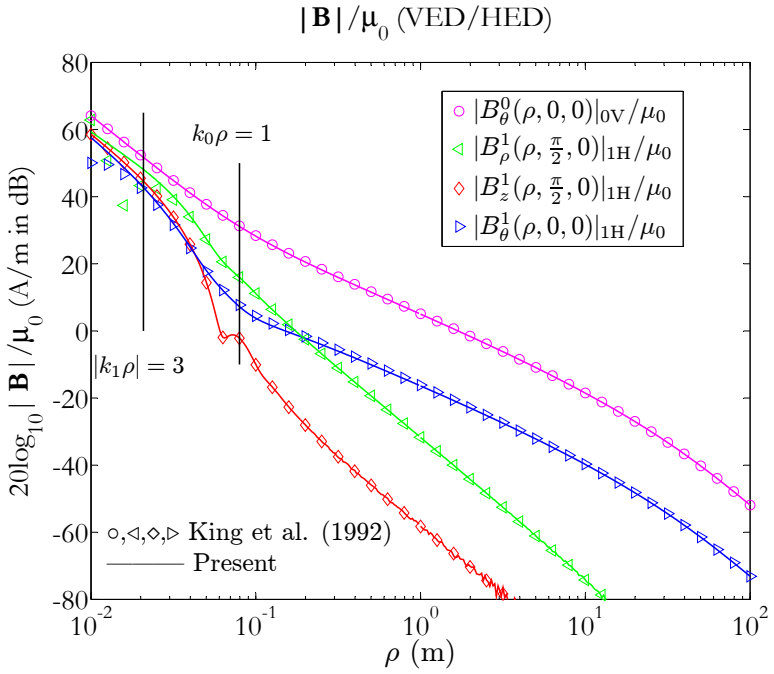

Figure 3.7: Magnetic fields due to separate VED and HED radiation.

line between the near-field and intermediate-field responses.

The second example deals with the four-layer system depicted in Fig. 3.8 with $\varepsilon_1 = 2\varepsilon_0$, $\varepsilon_2 = 10\varepsilon_0$, $\varepsilon_3 = \varepsilon_0$, $\sigma_j = 0$ $(j = 0, 1, 2, 3)$, $\mu_1 = 0.8\mu_0$, $\mu_2 = 1.2\mu_0$, and $\mu_3 = \mu_0$ as in [29] (note that $\epsilon_{\rm o} = \varepsilon_2$ and $\mu_{\rm o} = \mu_2$ in this case). Each of the two "internal" layers, sandwiched between the half-spaces, is 500 nm thick ($h_1 = h_2 = 0.5\,\mu$m). With reference to Fig. 3.2, the point source is located on the z-axis in the upper half-space, 500 nm above z_0, so that $\ell = 0$ and $s = z_0 - 0.5\,\mu$m. The results are plotted along the axial line $\{(\rho, \theta, z) :\ \theta = 0, \rho = 750\,\text{nm}\}$. Similar to the previous example, the results are computed assuming either VED or HED in the x-direction (for which $\theta_0 = 0$ in (3.49)), each acting at frequency 473.93 THz. As an illustration, Fig. 3.9(a) shows the magnitude of the E_x and E_z electric field components due to VED, while Fig. 3.9(b) plots $|E_x|$, $|E_y|$ and $|E_z|$ generated by HED. In both panels, the result of present calculations is compared to those in [22], [29] and [30]. Again, the agreement between the results is good, thus verifying the fidelity of the proposed analytical and computational treatment.

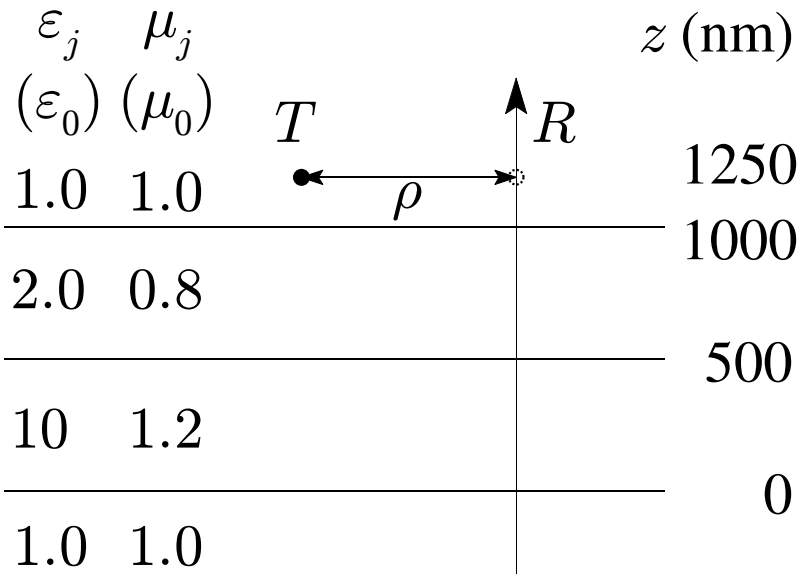

Figure 3.8: Four-layer medium, $\rho = 750$ nm.

3.6 Conclusion

In this chapter, a complete set of 3D layered electromagnetic Green's functions is derived by way of the TE and TM scalar potentials, featuring a new "direct" formulation for the *field forms* of the spectral Green's functions. To compute the corresponding point-load solutions in the spatial domain accurately and efficiently, the resulting improper integrals are evaluated via the method of asymptotic decomposition, wherein the featured singular behaviors are extracted and integrated analytically, while the residual components are computed via the method of adaptive numerical contour integration. In doing so it is found that, in the spectral

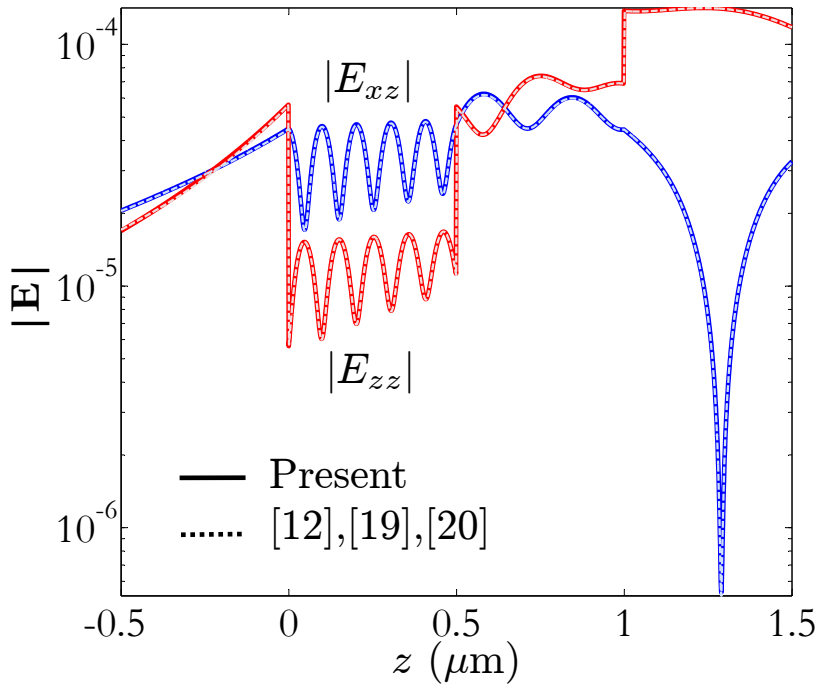

(a)

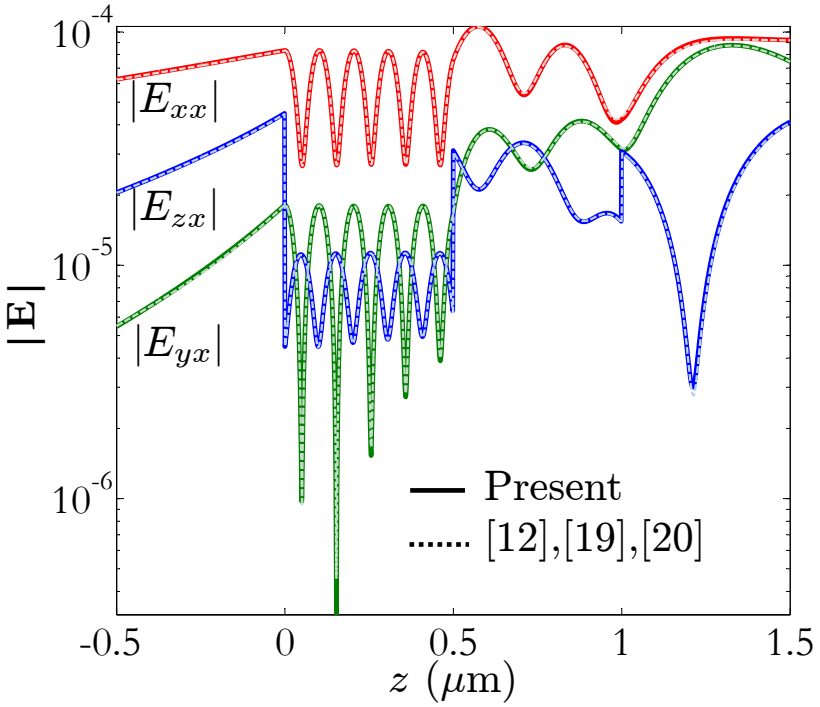

(b)

Figure 3.9: **E** field due to (a) VED and (b) HED in a four-layer medium.

domain, the decay of the (numerically-integrated) *residual* field forms is commensurate to that of their potential-form counterparts, which eliminates the perceived gap between the computation of the field forms and respective potential forms of the Green's functions in the spatial domain. The effectiveness and accuracy of the proposed methodology is evaluated via comparison with relevant examples in the literature. The proposed analytical and computational platform may bear particular relevance to the method-of-moments computations (such as those featured by the EFIE/MFIE methods) involving the field forms of the electromagnetic Green's functions.

Chapter 4

Full Waveform Back-analysis

4.1 GPR Equipment

The GPR equipment (Fig. 4.1) used in this study is model 4108 air-coupled 1 GHz modified bowtie antennas, manufactured by Geophysical Survey Systems, Inc. (GSSI). Model 4108 is configured as a bistatic antenna system, with dedicated transmitter and receiver antennas positioned at the same elevation and the apertures face downward.

In general, without taking into account the complex geometry of the modified bowtie antenna, the aperture surface can be simplified as a horizontal electric dipole (HED) antenna, given that the pavement is located at a sufficient distance

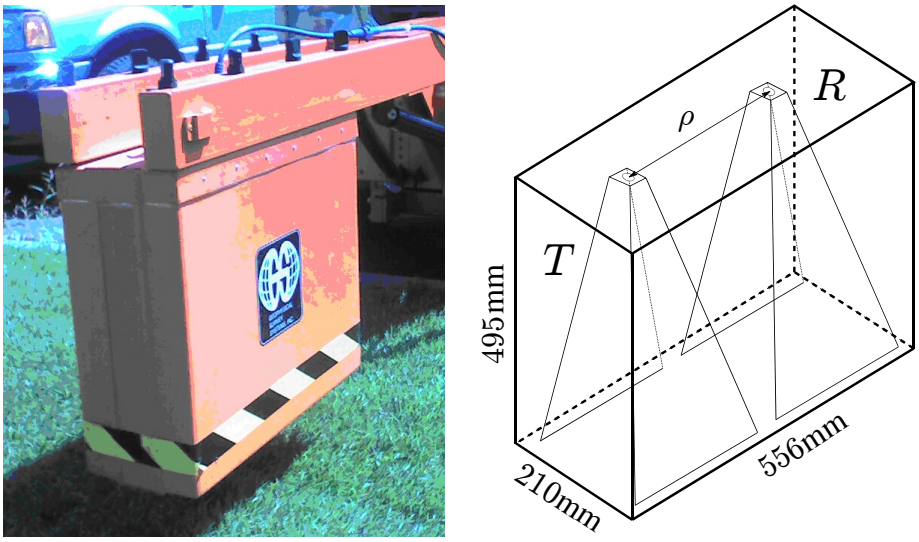

Figure 4.1: Model 4108 1 GHz air-coupled GPR [1].

from the antenna. The so-called far-field region can be estimated by

$$r \geq 2D^2/\lambda, \tag{4.1}$$

where D is the maximum overall dimension (aperture width) and λ is the wavelength of the electromagnetic wave [31]. Since the overall size of the GPR box is $210 \times 556 \times 495$ mm, a reasonable estimate of D for each antenna is 0.25 m, and the wavelength of a 1 GHz electromagnetic wave in air is $\lambda = 0.3$ m. Guided by these two conditions, the far-field is determined as the region with a radial distance beyond 0.4 m. Because the GPR box is placed at approximately 0.5 m above the ground, the whole pavement system satisfies the far-field condition, allowing the actual antenna to be modeled by the HED antenna. In other words, the GPR system can be simplified as two HED antennas over the pavement, as

shown in Fig. 4.2.

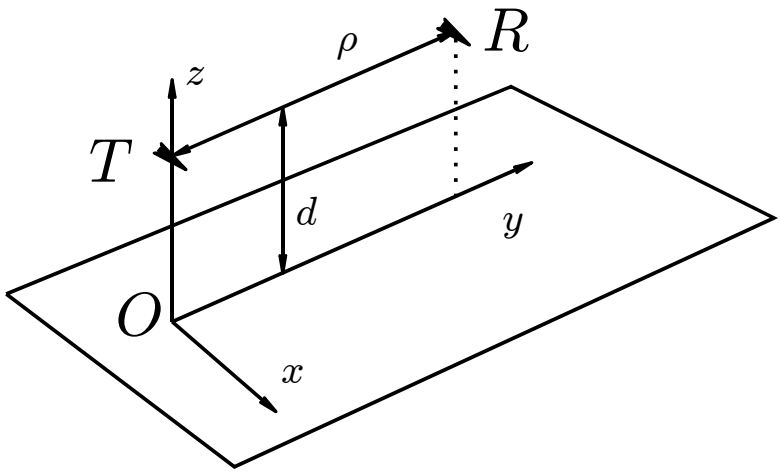

Figure 4.2: Two x-directed HED antennas, transmitter (T) and receiver (R).

4.2 GPR simulation

Under the assumed configuration (Fig. 4.2), GPR measures the x-component of the electric field at point R due to an x-directed HED at point T. In this study, a three-layer pavement system (air, asphalt, and base layers) is investigated. As shown in Fig. 4.3, each layer is characterized by the thickness h_j, dielectric constant ϵ_j, permeability μ_j and conductivity $\sigma_j (j = 0, 1, 2)$, where the air and base layers are two half-spaces, *i.e.* $h_0 = h_2 = \infty$. For the asphalt and base layers, the variation of the parameters is shown in Table 4.1. Note that $\epsilon_0 = 8.8542 \times 10^{-12}$ F/m, $\mu_0 = 4\pi \times 10^{-7}$ N/A^2 and $\sigma_0 = 0$ S/m in region 0 (air).

The wave number for each region is defined as $k_j = \omega\sqrt{\mu_j \widetilde{\epsilon}_j}$, where $\widetilde{\epsilon}_j = \epsilon_j + i\sigma_j/\omega$ and $\omega = 2\pi f$ is the angular frequency. For a three-layer system, the analytic solution of the electric field due to an electric HED in the air is available in the literature [25].

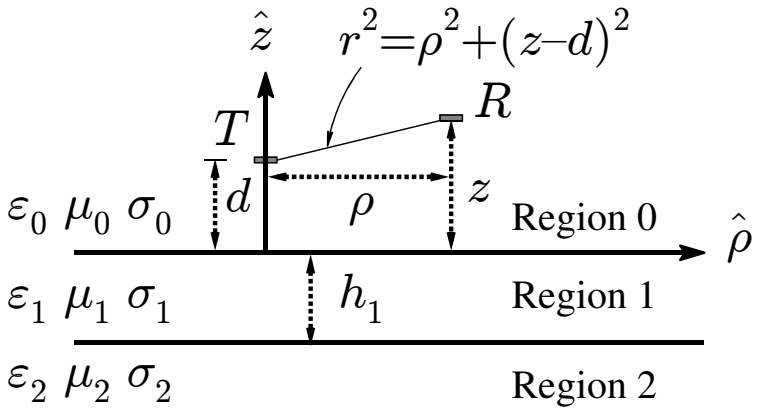

Figure 4.3: Three-layer system.

Table 4.1: Parameter Ranges

	Asphalt Region 1	Base Region 2
ϵ_j(F/m)	$3\epsilon_0 \sim 12\epsilon_0$	$4\epsilon_0 \sim 20\epsilon_0$
μ_j(N/A^2)	μ_0	μ_0
σ_j(S/m)	$10^{-4} \sim 10^{-1}$	$10^{-4} \sim 10^{-1}$

As detailed in Chapter 3, the electromagnetic Green's function (*i.e.* field induced by a point source) in the layered system can be computed analytically, represented by $E_\rho(\mathbf{r}, \omega)$ and $E_\theta(\mathbf{r}, \omega)$, with $\mathbf{r} = (\rho, \theta, z)$ and $\rho = \sqrt{x^2 + y^2}, \cos\theta = x/\rho, \sin\theta = y/\rho$. Furthermore, the x-component of the received HED is obtained

by trigonometric relations from E_ρ and E_θ via

$$\begin{aligned} E_x(\mathbf{r},\omega) &= E_\rho(\mathbf{r},\omega)\cos\theta - E_\theta(\mathbf{r},\omega)\sin\theta, \\ E_y(\mathbf{r},\omega) &= E_\rho(\mathbf{r},\omega)\sin\theta + E_\theta(\mathbf{r},\omega)\cos\theta. \end{aligned} \tag{4.2}$$

The Green's function in (4.2) can be thought of as the frequency response function associated with certain pavement systems. Thus, using the x-component of the Green's function in (4.2), the GPR measurements (in time domain) $\widetilde{G_x}(\mathbf{r},t)$ can be generated via the inverse Fourier transform $F^{-1}[X]$:

$$\widetilde{G_x}(\mathbf{r},t) = F^{-1}[G_x(\mathbf{r},\omega)], \tag{4.3}$$

where

$$G_x(\mathbf{r},\omega) = E_x(\mathbf{r},\omega)\cdot I(\omega) \tag{4.4}$$

is the GPR response in the frequency domain. The $I(\omega)$ in (4.4) represents the signature of the excitation current source, which varies from different GPR antennas [32].

Therefore, by using the layered electromagnetic wave propagation model, synthetic GPR time histories for an asphalt-base configuration can be generated. For example, the GPR measurement over a three-layer pavement system is shown in Fig. 4.4. It is worth noting that the direct arrival is not shown because it contains no information about the pavement profile. The first echo is the reflection

from the surface; the second echo is the reflection from the interface between the asphalt and base layer.

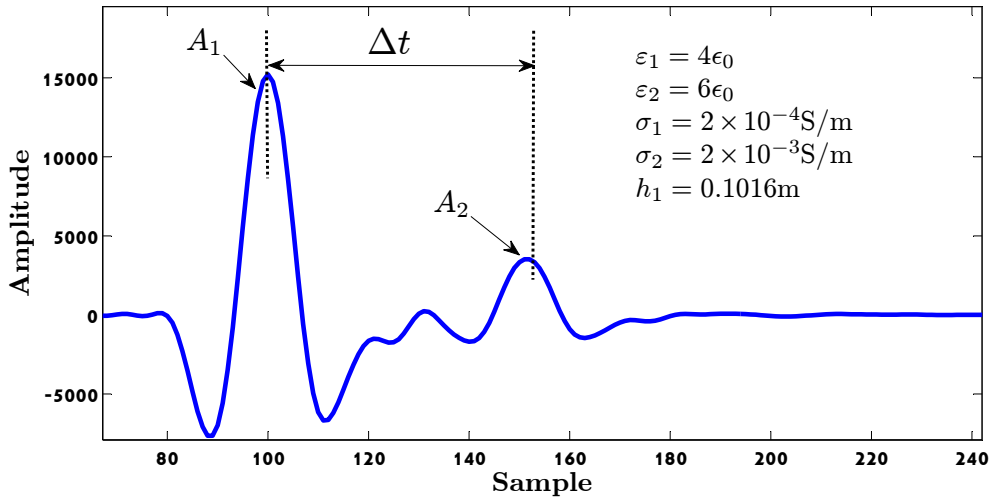

Figure 4.4: Synthetic GPR scan.

In addition, it may be observed from (4.4) that the characteristic of each echo is strictly associated with the current source and the peak amplitude. Since the current source is fixed, the peak amplitude can be used to represent the overall reaction of the impulse due to the layer properties such as dielectric constant and conductivity. Assuming constant conductivities, it can be further observed that the amplitude of the first peak A_1 is solely determined by the dielectric constant of the asphalt layer ϵ_1. Consequently, the amplitude of the second peak A_2 is not only affected by the dielectric constants of the base layer ϵ_2, but also affected by ϵ_1 in the asphalt layer. Moreover, the travel time Δt represented by the distance

between the first and second peaks will be affected by the variation of wave speed due to the variational dielectric constant of the asphalt layer ϵ_1. In other words, the travel time Δt is co-determined by both ϵ_1 and h_1. Mathematically, the above observations can be described by the following formulas:

$$A_1 = f_1(\epsilon_1), \quad A_2 = f_2(\epsilon_1, \epsilon_2), \quad \Delta t = f_3(\epsilon_1, h_1), \tag{4.5}$$

where the anonymous functions f_1, f_2, and f_3 can be evaluated from the Green's function in (4.2).

4.3 Optimization of Synthetic GPR Scan

For the three-layer configuration, the GPR time history is uniquely characterized by all three parameters, namely A_1, A_2, and Δt (Fig. 4.4). Comparing the synthetic GPR scan to the measured one, it is found that it is possible to generate a synthetic GPR scan identical to the measured GPR scan by fitting the layer properties (thickness and dielectric constant) to the actual field values. For example, as shown in Fig. 4.5, no major differences can be recognized between the measured and the fitted synthetic GPR scans. Thus, it is intuitive to interpret the layer properties by using a certain optimization scheme to fit the synthetic GPR scan to every measured GPR scan.

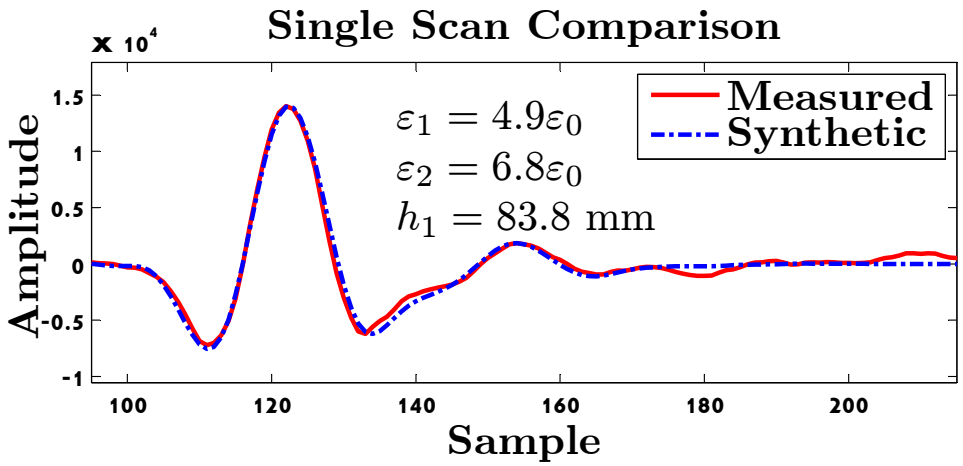

Figure 4.5: The measured and the fitted synthetic GPR scan.

The optimization scheme is developed following (4.5), with the objective functions introduced as

$$\begin{aligned} g_1(\epsilon_1) &= A_1 - A_1^{\text{field}} = f_1(\epsilon_1) - A_1^{\text{field}}, \\ g_2(\epsilon_1, \epsilon_2) &= A_2 - A_2^{\text{field}} = f_2(\epsilon_1, \epsilon_2) - A_2^{\text{field}}, \\ g_3(\epsilon_1, h_1) &= \Delta t - \Delta t^{\text{field}} = f_3(\epsilon_1, h_1) - \Delta t^{\text{field}}, \end{aligned} \tag{4.6}$$

which means that the closer the parameters (ϵ_1, ϵ_2 and h_1) to their objective values in the field, the smaller are the three objective functions in (4.6). It is worth noting that in (4.6), it is not necessary to fit the dielectric constant ϵ_1 in the second or third equations, which is obtained from the fitted result of the first equation. Thus, the task is simplified to find the root of a single variable function for all three objective functions.

4.4 GPR Survey

To evaluate the proposed scheme, experiments were performed to compare the estimated layer thicknesses with sample cores from the MnRoad facility. A total of 11 cores were taken from different cells in the MnRoad low volume road section, with a typical 80-130 mm asphalt layer over the base material. The core data are shown in Table 4.2.

Table 4.2: MnRoad Sample Core Thickness Information

Core #	MnRoad ID	Cell	Station	Thickness (mm)
1	3509BC006	35	7496	114
2	3409BC006	34	7444	127
3	3307BC006	33	6562	111
4	3309BC006	33	6374	114
5	2409BC012	24	15821	89
6	2409BC003	24	16326	89
7	2808BC001	28	18148	111
8	2808BC003	28	18350	102
9	7909BC002	79	19618	95
10	7909BC007	79	19741	114
11	3507BC005	35	7702	102

GPR surveys were conducted, and the scans were marked at the core locations. The marked scans were used to interpret the layer thicknesses using the proposed optimization scheme. The estimated asphalt layer thicknesses are shown

in Table 4.3, as well as the errors compared to the core data, *i.e.*

$$\text{Error}(\%) = \frac{|h - h^{\text{est}}|}{h} \times 100\%, \tag{4.7}$$

where h is core thickness and h^{est} is the estimated thickness using the proposed scheme. From Table 4.3, the highest error is 6.9%, with a considerably lower average of 2.3%. Moreover, it is important to notice that 7 out of 11 scans have errors less than or equal to 1.1%.

Table 4.3: Compare Layer Thickness Estimation with Sample Core Data

Core #	Thickness (mm)	Estimated (mm)	Error (%)
1	114	107	6.1
2	127	128	0.8
3	111	110	0.9
4	114	109	4.4
5	89	90	1.1
6	89	92	3.4
7	111	111	0.0
8	102	109	6.9
9	95	94	1.1
10	114	114	0.0
11	102	101	1.0

The proposed scheme is also capable of providing thickness and dielectric constant profiles from GPR surveys under highway speed. As an illustration, one GPR survey completed by MnDOT was processed by the proposed method. The test site is a section of pavement consisting of a HMA layer and underlying base.

The survey was performed at 9.8 scan/m over 200 m with a driving speed of 100 km/h.

Using the proposed interpretation scheme, the obtained layer properties (ϵ_1, ϵ_2 and h) are shown in Fig. 4.6, where the asphalt thickness variation can be clearly quantified with an average of 91 mm. The results indicate a variation of the asphalt dielectric constant from $3.5\epsilon_0 \sim 7.8\epsilon_0$. As a result, it shows the utility of the method in interpreting pavement layer properties without a priori assumptions. Particularly, the interpreted asphalt thickness is compared to that using the traditional travel time technique, with the commonly assumed asphalt dielectric constant of $\epsilon_1 = 6\epsilon_0$. As shown in Fig. 4.7, the pavement thickness interpreted from the travel time technique contains an average error of 7.6%, with a maximum error of 25%.

Furthermore, the synthetic GPR image can be produced directly from the interpreted parameters, exhibiting strong similarity to the measured GPR image, as shown in Fig. 4.8. As a matter of fact, the measured GPR image may be contaminated by other activities such as the interference from a cell phone signal. On the other hand, the synthetic GPR scan can be generated without any noise, which offers an enhanced visualization, *i.e.* by removing the ambient noise in the GPR scans, the GPR image becomes less fuzzy and hence during the interpretation of the pavement profile, misidentification can be reduced.

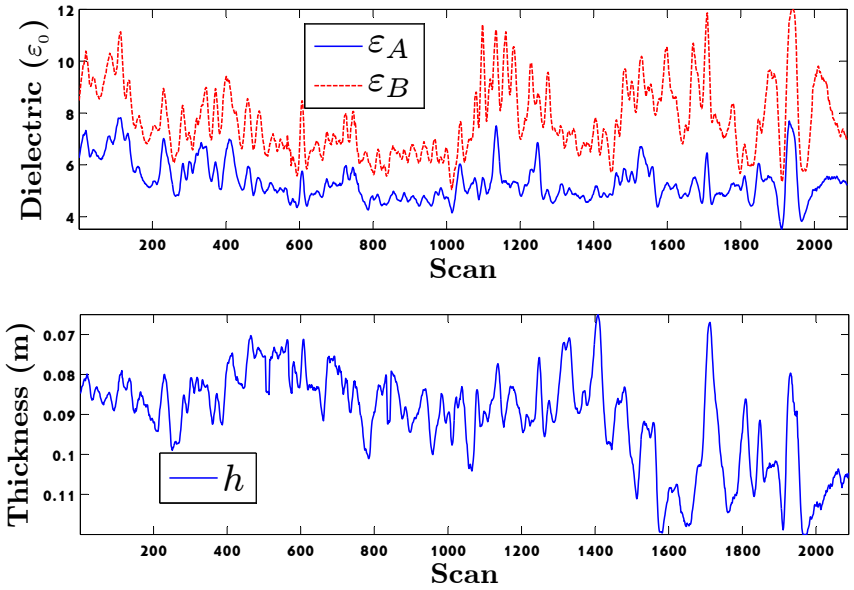

Figure 4.6: Road profile summary.

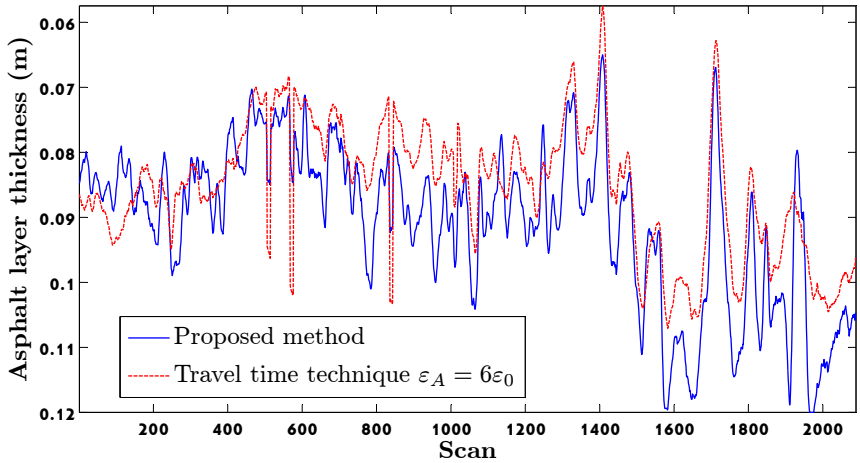

Figure 4.7: Estimated thickness using the proposed method and travel time technique

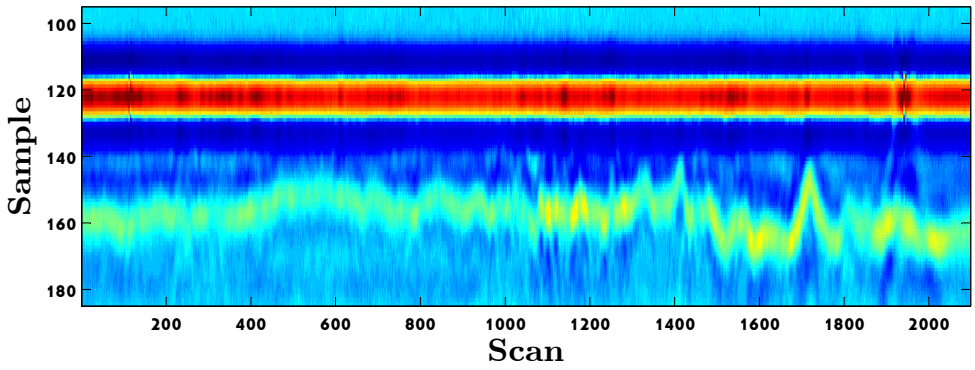

(a) Measured GPR image

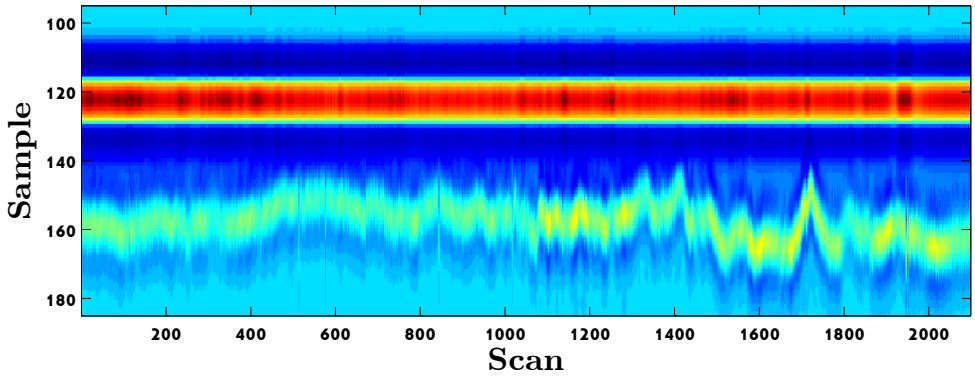

(b) Synthetic GPR image

Figure 4.8: GPR images: (a) measured and (b) synthetic.

4.5 Conclusion

By using the analytic representation of the electromagnetic Green's function in a layered system, the GPR scans are successfully simulated over a wide range of pavement profiles. Based on this forward model, an interpretation scheme to estimate the layer thickness without a priori assumption of the pavement condition is proposed. The interpreted layer thickness shows very low error compared to

the sample core data, indicating the success of this proposed scheme. The results also show the validation of the proposed scheme to process GPR measurements obtained at highway speeds.

Chapter 5

Summary

The purpose of this study is to extend the use of GPR methodology towards more reliable and accurate interpretation of pavement conditions. The study contains two parts: i) the forward modeling of the electromagnetic wave propagation in the layered pavement system, and ii) the back-analysis scheme based on full waveform to interpret the GPR measurements. Several highlights are listed below.

1. By solving the Maxwells equations in a layered medium, a complete set of 3D layered EM Green's functions is derived using the integral transform method by way of transverse electric and transverse magnetic scalar potentials, featuring a new direct formulation for the field forms of the EM Green's functions (in spatial domain). In the literature, the field forms of the EM vectors are usually computed via numerical differentiation (with respect to

x,y,z) on the field forms of their potential (*i.e.* magnetic vector potential in spatial domain) in integral forms. In contrast, the differentiation in the new approach is done under the integral sign which results in a more stable and accurate computation since i) the differentiation of the potential form kernels (in spectral domain) is done in closed-form *i.e.* exactly, and ii) one can explicitly control the accuracy of numerical integration of such differentiated kernels.

2. The improper integrals underpinning the computation of the corresponding point-load solutions (in spatial domain) are evaluated via the method of asymptotic decomposition, wherein the singular behaviors are entirely extracted and integrated analytically – so that the remaining residual components can be computed effectively and accurately via adaptive numerical quadrature. It is also found that, in the spectral domain, the decay of the (numerically-integrated) residual from the field forms is commensurate to that of their potential form counterparts, which eliminates the perceived gap between the computation of the field forms and respective potential forms of the Green's functions in the spatial domain. The effectiveness and accuracy of the proposed methodology is evaluated via comparison with relevant examples in the literature.

3. In terms of numerical integration, the implementation is self-adaptive as it increases the integration (*i.e.* quadrature) density when and where needed. The issue of self-adaptivity is important when dealing with arbitrary layering configurations over a wide spectrum of frequencies. In this case, the kernels of the featured (improper) integrals are known to vary widely, and using a "one size fits all" grid of quadrature points along the selected contour path may not be the most effective (nor robust) way to tackle the problem.

4. Utilizing the electromagnetic Greens function for a layered system due to a horizontal electric dipole, the air-coupled GPR scan can be successfully simulated over a wide range of pavement profiles. By virtue of this simulation, the best match of the GPR scan in terms of full waveform can be found within thousands of simulations via the optimization routine, where the layer parameters associated with the measurement are equal to the simulation inputs.

5. The accuracy of the interpreted layer thickness from the new scheme is verified by the ground truth, with average error of 2.3% compared to the 7.5% average error of the traditional method. Unlike the traditional method, the new back-analysis scheme is provided on a more rigorous basis, which allows an evaluation of the relevant pavement properties with no prior assumptions.

6. Last but not least, the forward model can be applied to simulate various kinds GPR device, provided that the GPR system can be approximated by point source(s).

In the future, this interpretation scheme could be developed further to be able to accomendate for pavement structures with more than three layers as illustrated here, since the simulation and back-analysis scheme is capable to be applied to n-layer system ($n > 3$). Meanwhile, the *in-situ* dielectric is also provided along with the thickness interpretation, which could lead to the interpretation of other important pavement properties such as moisture content and void ratio. It is important to realize the potential to obtain the multivariable profiles along the road, which is essential to establish a quantitative network-level pavement monitoring.

References

[1] R. Dr. Roberts (GSSI Inc.). Personal communication, Jan. 2010.

[2] Y. Hachiya and K. Sato. Effect of tack coat on bonding characteristics at interface between asphalt concrete layers. *Proceedings of 8th International Conference on Asphalt Pavements*, vol. 1, 1997.

[3] M. R. Kruntcheva, A. C. Collop, and N. H Thom. Effect of bond condition on flexible pavement performance. *ASCE Journal of Transportation Engineering*, 131/11, Nov. 2005.

[4] Imad L. Al-Qadi, Samer Lahouar, and Amara Loulizi. *Ground-penetrating radar calibration at the Virginia Smart Road and signal analysis to improve prediction of flexible pavement layer thicknesses.* Virginia Transportation Research Council, 2005.

[5] David J. Daniels. *Ground penetrating radar*. Institution of Electrical Engineers, 2004.

[6] Timo Saarenketo and Thomas Scullion. *Ground penetrating radar applications on roads and highways*. Texas Transportation Institute, Texas A & M University System, 1994.

[7] Timo Saarenketo and Tom Scullion. Road evaluation with ground penetrating radar. *Journal of Applied Geophysics*, 43(2-4):119–138, 2000.

[8] Samer Lahouar, Imad L. Al-Qadi, Amara Loulizi, Trenton M. Clark, and David T. Lee. Approach to determining in situ dielectric constant of pavements: Development and implementation at interstate 81 in virginia. *Transportation Research Record*, (1806):81–87, 2002.

[9] Kenneth R. Maser. Measurement of as-built conditions using ground penetrating radar. *Structural materials technology : an NDT conference.*, 1996.

[10] Yuejian Cao, Shongtao Dai, Joseph Labuz, and John Pantelis. Implementation of ground penetrating radar. *Minnesota Department of Transportation, Research Services Section*, Aug. 2007.

[11] Weng C. Chew. *Waves and Fields in Inhomogeneous Media*. Van Nostrand Reinhold, New York, 1990.

[12] Tie J. Cui, Werner Wiesbeck, and Alexander Herschlein. Electromagnetic scattering by multiple three-dimensional scatterers buried under multilayered media - Part I: Theory. *IEEE Transactions on Geoscience and Remote Sensing*, 36(2):526–534, 1998.

[13] K. A. Michalski and D. Zheng. Electromagnetic scattering and radiation by surfaces of arbitrary shape in layered media. I. Theory. *IEEE Transactions on Antennas and Propagation*, 38(3):335–344, 1990.

[14] K. A. Michalski. Formulation of mixed-potential integral equations for arbitrarily shaped microstrip structures with uniaxial substrates. *Journal of Electromagnetic Waves and Applications*, 7(7):899–917, 1993.

[15] K. A. Michalski and J. R. Mosig. Multilayered media Green's functions in integral equation formulations. *IEEE Transactions on Antennas and Propagation*, 45(3):508–519, 1997.

[16] Leung Tsang, Chong-Jin Ong, Chung-Chi Huang, and V. Jandhyala. Evaluation of the Green's function for the mixed potential integral equation (MPIE) method in the time domain for layered media. *IEEE Transactions on Antennas and Propagation*, 51(7), 2003.

[17] Arnold Sommerfeld. *Partial Differential Equations in Physics*. Academic Press, New York, 1964.

[18] Wei Cai and Tiejun Yu. Fast calculations of dyadic Green's functions for electromagnetic scattering in a multilayered medium. *Journal of Computational Physics*, 165(1):1–21, Nov. 2000.

[19] P. Yla-Oijala, M. Taskinen, and J. Sarvas. Multilayered media Green's functions for MPIE with general electric and magnetic sources by the Hertz potential approach - abstract. *Journal of Electromagnetic Waves and Applications*, 15(7):913–914, 2001.

[20] Tiejun Yu and Wei Cai. FIFA – Fast interpolation and filtering algorithm for calculating dyadic Green's function in the electromagnetic scattering of multilayered structures. *Communications in Computational Physics*, 1(2):229–260, 2006.

[21] Tie J. Cui and Weng C. Chew. Fast evaluation of Sommerfeld integrals for EM scattering and radiation by three-dimensional buried objects. *IEEE Transactions on Geoscience and Remote Sensing*, 37(2):887–900, 1999.

[22] E. Simsek, Q. H. Liu, and B. Wei. Singularity subtraction for evaluation of Green's functions for multilayer media. *IEEE transactions on microwave*

theory and techniques., 54(1):216, 2006.

[23] Roger F. Harrington. *Time-harmonic Electromagnetic Fields*. IEEE Press : Wiley-Interscience, New York, 2001.

[24] H. A. Erdelyi, editor. *Tables of Integral Transforms, Volume II: based, in part, on notes left by Harry Bateman*. McGraw-Hill, New York, 1954.

[25] Ronold W. P. King, Margaret Owens, and Tai T. Wu. *Lateral Electromagnetic Waves: Theory and Applications to Communications, Geophysical Exploration, and Remote Sensing*. Springer-Verlag, 1992.

[26] B. B. Guzina and R. Y. S. Pak. On the analysis of wave motions in a multilayered solid. *Quarterly Journal of Mechanics and Applied Mathematics*, 54:13–37, 2001.

[27] Robert G. Hunsperger. *Integrated Optics: Theory and Technology*. Springer, Berlin, New York, 1995.

[28] Milton Abramowitz and Irene A. Stegun. *Handbook of Mathematical Functions with Formulas, Graphs, and Mathematical Tables*. U.S. Govt. Print. Off., Washington, 1964.

[29] M. Paulus, P. Gay-Balmaz, and O. J. F. Martin. Accurate and efficient computation of the Green's tensor for stratified media. *Physical Review E*, 62:5797–5807, 2000.

[30] E. Prof. Simsek. Personal communication. 2010.

[31] Constantine A. Balanis. *Antenna theory : analysis and design*. John Wiley & Sons, New York, second edition, 1997.

[32] Yuejian Cao, Bojan B. Guzina, and Joseph F. Labuz. *Pavement evaluation using ground penetrating radar*. Minnesota Department of Transportation, Research Services Section, 2008.